

Locally enhanced Voronoi cell finite element model (LE-VCFEM) for simulating evolving fracture in ductile microstructures containing inclusions

Chao Hu and Somnath Ghosh^{*,†}

*Department of Mechanical Engineering, The Ohio State University, 201 West 19th Avenue,
Columbus, OH 43210, U.S.A.*

SUMMARY

Ductile heterogeneous materials such as cast aluminum alloys undergo catastrophic failure that initiates with particle fragmentation, which evolves with void growth and coalescence in localized bands of intense plastic deformation and strain softening. The Voronoi cell finite element model (VCFEM), based on the assumed stress hybrid formulation, is unable to account for plastic strain-induced softening. To overcome this shortcoming of material softening due to plastic strain localization, this study introduces a locally enhanced VCFEM (LE-VCFEM) for modeling the very complex phenomenon of ductile failure in heterogeneous metals and alloys. In LE-VCFEM, finite deformation displacement elements are adaptively added to regions of localization in the otherwise assumed stress-based hybrid Voronoi cell finite element to locally enhance modeling capabilities for ductile fracture. Adaptive h -refinement is used for the displacement elements to improve accuracy. Damage initiation by particle cracking is triggered by a Weibull model. The nonlocal Gurson–Tvergaard–Needleman model of porous plasticity is implemented in LE-VCFEM to model matrix cracking. An iterative strain update algorithm is used for the displacement elements. The LE-VCFEM code is validated by comparing with results of conventional FE codes and experiments with real materials. The effect of various microstructural morphological characteristics is also investigated. Copyright © 2008 John Wiley & Sons, Ltd.

Received 26 February 2008; Revised 9 May 2008; Accepted 13 May 2008

KEY WORDS: Voronoi cell finite element model; ductile fracture; matrix cracking; nonlocal Gurson–Tvergaard–Needleman model; void coalescence

*Correspondence to: Somnath Ghosh, Department of Mechanical Engineering, The Ohio State University, 201 West 19th Avenue, Columbus, OH 43210, U.S.A.

†E-mail: ghosh.5@osu.edu

Contract/grant sponsor: National Science Foundation NSF Div Civil and Mechanical Systems Division; contract/grant number: CMS-0308666

Contract/grant sponsor: Department of Energy Aluminum Visions Program; contract/grant number: A5997

Contract/grant sponsor: Ohio Supercomputer Center; contract/grant number: PAS813-2

1. INTRODUCTION

Many metals and alloys, e.g. cast aluminum *A319* used in automotive, aerospace and other engineering systems, consist of heterogeneities in the form of particulates, fibers or precipitates. These heterogeneities often have adverse effects on their failure properties such as ductility and fracture toughness. Major microstructural mechanisms that are responsible for deterring these properties include particulate fragmentation, interfacial debonding and matrix failure [1–3]. Ductile failure initiates with particle cracking or interfacial debonding. Voids grow near the crack tips with deformation and subsequently coalesce with neighboring voids to result in matrix failure. Evolution of matrix failure causes microstructural stress redistribution that leads to cracking of other particles. Eventually, the phenomenon leads to catastrophic failure of the microstructure. Crack initiation and propagation mechanisms are sensitive to micromechanical state variables, especially stress triaxiality and plastic deformation. Experimental studies on ductile failure, e.g. in [4–7], have shown strong connections between morphological variations and microstructural damage nucleation. Modeling failure properties such as strain to failure and ductility requires incorporation of microstructural morphology for accurate prediction.

A number of analytical, computational and experimental studies have been conducted to model ductile failure, e.g. [8–11] in plastic materials. A widely used phenomenological continuum damage constitutive law for a progressively cavitating solid has been introduced by Gurson [12]. This model has been augmented to account for the loss of load-carrying capacity through void coalescence in the widely popular Gurson–Tvergaard–Needleman (GTN) models in [13]. Various extensions to this model have been suggested in the literature, e.g. for void shape effects in [14–16], for rate- and temperature-dependent effects in [17], and for effects of anisotropy on plastic flow in [14, 18]. Void nucleation, which can occur at second-phase particles through particle debonding and/or particle cracking, is the first stage of ductile fracture. For void nucleation, ‘stress-controlled’ nucleation criteria have been proposed in [19–21], whereas ‘strain-controlled’ nucleation criteria have been developed in [22]. Void coalescence shifts a relatively homogeneous deformation state to a highly localized one in the microstructure. A model for void coalescence using acceleration functions [23] has been shown to work well for low stress triaxiality in [24]. Studies on void coalescence with elastic–viscoplastic GTN model, accounting for void shape evolution, coalescence and post-coalescence micromechanics, have been conducted in [14, 25]. For avoiding the inherent mesh sensitivity of numerical failure predictions, a nonlocal evolution equation for the void volume fraction has been proposed for the GTN models in [23, 26]. A material characteristic length is directly incorporated into the constitutive relation as an additional phenomenological parameter. This model is used in the present paper to model ductile fracture.

A large volume of computational studies have been conducted for understanding the ductile damage behavior of heterogeneous materials during elastic–plastic deformation [27–33]. The predictive capability of unit cell models for failure properties in nonuniform microstructures is limited due to simplification of the critical local features, necessary to model strain to failure. Additionally, many of these studies focus only on the initial stages of ductile damage and have not considered the effect of microstructural morphology on the evolution of ductile failure by void growth in the matrix and coalescence beyond particle fracture. There is a paucity of studies on failure modeling in the presence of reinforcements of arbitrary shapes, sizes, orientation and nonuniform spatial distribution, which range all the way from nucleation through complete failure. Ductile fracture depends on extreme values of microstructural characteristics, e.g. nearest-neighbor

distance (NND), rather than the low-order moments such as mean volume fraction. Hence, it is particularly important to accurately represent the real microstructural characteristics in the models.

A problem that has conventionally plagued successful FE modeling of evolving cracks is the lack of adequate resolution and topology description that should typically follow the crack path. Evolving discontinuities such as cracks have been handled in computational modeling through specialized explicit and implicit modeling techniques. In the explicit models, discontinuous displacements are constructed along distinct surfaces of strong discontinuities or cracks, whereas in the implicit models, discontinuous strain or stress fields represent regions of diffused cracking. Significant advances have been made in the modeling of propagation of strong and weak discontinuities with these approaches, based on the incorporation of embedded discontinuities in the element displacement or strain fields. A cogent review of some of these methods is provided in [34]. Cohesive zone models [35–37] have emerged as important tools for modeling crack propagation by lacing the interface between contiguous elements with cohesive springs. However, very often these models require highly refined computational mesh to control the direction of crack propagation. Frequent remeshing and mapping crack propagation is time consuming and yields poor computational efficiency. To avert this, intra-element enrichment approaches have been proposed to eliminate mesh dependence of crack path. Elements with embedded discontinuities based on enhanced strain formulations have been proposed in [38] for capturing discontinuities across the FE mesh and in [39, 40] for modeling softening in the interior of an element. The concept of enhanced strain element using a three-field mixed formulation has been introduced in [41–43]. The extended FEM in [44–46] uses the partition of unity concept for incorporating local enrichment functions for modeling cohesive crack propagation, while preserving the general displacement-based FEM formalism.

Studies conducted by Ghosh *et al.* have focused on modeling more realistic representation of microstructures with nonuniform dispersion of heterogeneities [2] by combining digital image processing with microstructure modeling. The present study extends the microstructural Voronoi cell FE model or VCFEM developed by Ghosh and co-workers [3, 47–51] to model ductile fracture in heterogeneous microstructures of ductile alloys from nucleation to final failure. VCFEM has been demonstrated to offer significant promise accurate micromechanical analysis of arbitrary heterogeneous microstructures with high efficiency. Morphological arbitrariness in dispersions, shapes and sizes of heterogeneities, as seen in real micrographs, are readily modeled by this method. Earlier developments in ductile fracture of materials with VCFEM have been limited to microstructural damage inception by particle cracking only in [3, 51]. In the present study, a locally enhanced VCFEM or LE-VCFEM is developed to extend particle fragmentation into full blown ductile failure of the microstructure by matrix cracking in the form of void nucleation, growth and coalescence. In LE-VCFEM, the stress-based hybrid VCFEM formulation is enhanced adaptively in narrow bands of localized plastic flow and void growth. This region is overlaid with finite deformation, displacement-based elements to accommodate strain softening in the constitutive behavior. The LE-VCFEM is validated through comparisons with traditional computational models and experimental results. The effects of the material morphology on damage evolution are also examined in this study.

2. VCFEM FORMULATION FOR NONLOCAL POROUS PLASTICITY IN THE ABSENCE OF LOCALIZED INCLUSION AND MATRIX CRACKING

The VCFEM formulation is extended in this section for a porous elastic–plastic matrix, for which the constitutive behavior is represented by a rate-independent nonlocal GTN model [23, 26].

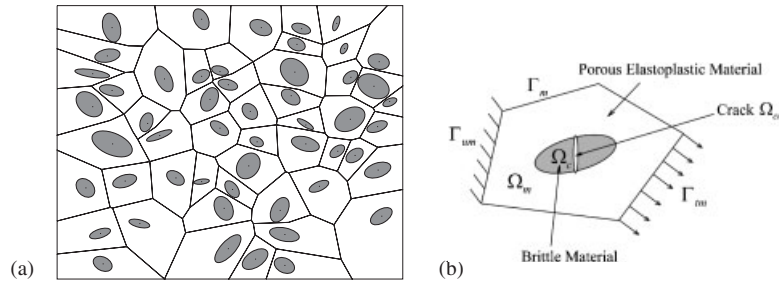


Figure 1. (a) Discretization of a multi-phase material microstructure into Voronoi cells by a tessellation method and (b) a typical Voronoi cell element with a cracked particle.

The model incorporates a strain update method for integrating porous elasto-plastic constitutive equations. In this section, the inclusions and particles in each Voronoi cell element are assumed to be uncracked.

2.1. Variational principle with assumed stress hybrid method

Consider a multi-phase material microstructural section shown in Figure 1(a). The microstructure is discretized into a network of N Voronoi cells by a tessellation process that accounts for location, size and shape of the N inclusions. Each cell represents the immediate neighborhood of an inclusion. As shown in Figure 1(b), the matrix and inclusion phases in each Voronoi cell are designated as Ω_m and Ω_c , respectively. A crack in the inclusion is labeled as Ω_{cr} and this will be discussed in Section 3. Each Voronoi cell containing matrix, inclusion and crack phases is designated as an element in the VCFE formulation, i.e. $\Omega_e = \Omega_m \cup \Omega_c \cup \Omega_{cr}$. The element boundary $\partial\Omega_e$ is assumed to be composed of a prescribed traction boundary Γ_{tm} , a prescribed displacement boundary Γ_{um} , and an interelement boundary Γ_m , i.e. $\partial\Omega_e = \Gamma_{tm} \cup \Gamma_{um} \cup \Gamma_m$. It is further assumed that these segments are mutually disjoint, i.e. $\Gamma_{tm} \cap \Gamma_{um} \cap \Gamma_m = \emptyset$. An incremental element energy functional Π_e^{ND} is defined for each Voronoi cell element without damage (represented by the superscript ND) in terms of stress increments in the matrix Ω_m , and inclusion Ω_c phases and displacement increments on the element boundary $\partial\Omega_e$, inclusion–matrix interface $\partial\Omega_c$. The energy functional Π_e^{ND} for each Voronoi cell element is expressed as

$$\begin{aligned}
 \Pi_e^{ND}(\Delta\sigma^m, \Delta\sigma^c, \Delta\mathbf{u}, \Delta\mathbf{u}') = & - \int_{\Omega_m} \Delta B(\sigma^m, \Delta\sigma^m) d\Omega - \int_{\Omega_m} \boldsymbol{\varepsilon}^m : \Delta\sigma^m d\Omega - \int_{\Omega_c} \Delta B(\sigma^c, \Delta\sigma^c) d\Omega \\
 & - \int_{\Omega_c} \boldsymbol{\varepsilon}^c : \Delta\sigma^c d\Omega + \int_{\partial\Omega_e} (\sigma^m + \Delta\sigma^m) \cdot \mathbf{n}^e \cdot (\mathbf{u} + \Delta\mathbf{u}) d\partial\Omega \\
 & - \int_{\Gamma_{tm}} (\bar{\mathbf{t}} + \Delta\bar{\mathbf{t}}) \cdot (\mathbf{u} + \Delta\mathbf{u}) d\Gamma \\
 & - \int_{\partial\Omega_c} (\sigma^m + \Delta\sigma^m - \sigma^c - \Delta\sigma^c) \cdot \mathbf{n}^c \cdot (\mathbf{u}' + \Delta\mathbf{u}') d\partial\Omega
 \end{aligned} \tag{1}$$

where ΔB is the increment of complimentary energy density, and the superscripts m and c correspond to variables associated with the matrix, inclusion and crack phases in each Voronoi cell

element. $\bar{\mathbf{t}}$ is the external traction on the traction boundary Γ_{tm} , and \mathbf{n} is the outward normal on respective boundary segments. \mathbf{u} and \mathbf{u}' are, respectively, the displacement degrees of freedom (DOFs) on the element boundary $\partial\Omega_e$ and interface $\partial\Omega_c$. Other variables in Equation (1) have been defined in [3, 51, 52]. The corresponding total energy functional for the entire computational domain is

$$\Pi^{\text{ND}} = \sum_{e=1}^N \Pi_e^{\text{ND}} \tag{2}$$

Setting the first variation of Π_e^{ND} with respect to stress increments $\Delta\boldsymbol{\sigma}^m$ and $\Delta\boldsymbol{\sigma}^c$ to zero, respectively, results in the kinematic equations of the matrix and inclusion phases as the Euler equations [47]. On the other hand, setting the first variation of Π_e^{ND} with respect to the independent boundary displacements $\Delta\mathbf{u}$ and $\Delta\mathbf{u}'$ to zero, respectively, yields the element boundary traction reciprocity and inclusion–matrix interface traction reciprocity conditions as the Euler equations, respectively.

In each Voronoi cell element, independent interpolations are made for equilibrated stress increments $\Delta\boldsymbol{\sigma}^m$ and $\Delta\boldsymbol{\sigma}^c$ in the matrix and inclusion phases. For two-dimensional problems, Airy’s stress function $\Phi(x, y)$ is used to derive equilibrated stress increments in each constituent phase. Stress functions are constructed for efficient computations and accuracy, accounting for two conditions in the choice of matrix stress functions:

- Effect of the inclusion shape should be dominant near the matrix–inclusion interface, but should vanish in the far field.
- Stress function construct should facilitate traction reciprocity across the interface.

For two-phase composites without any damage, Moorthy and Ghosh [47, 52] have constructed the matrix stress function as the sum of a purely polynomial function Φ_{poly}^m and a reciprocal function Φ_{rec}^m . The reciprocal stress function accounts for the shape of the interface $\partial\Omega_c$ through a parametric function $f(x, y)$, which transforms $\partial\Omega_c$ to a unit circle by the Schwarz–Christoffel conformal transformation [53]. The analytic function $f(x, y)$ represents a special radial coordinate with the property that $1/f(x, y) = 1$ on $\partial\Omega_c$ and $1/f(x, y) \rightarrow 0$ as $(x, y) \rightarrow \infty$. In the absence of a crack in the inclusion, the stress functions are constructed, respectively, as

$$\Phi^m = \Phi_{\text{poly}}^m + \Phi_{\text{rec}}^m, \quad \Phi^c = \Phi_{\text{poly}}^c \tag{3}$$

where

$$\Phi_{\text{poly}}^{m/c} = \sum_{p+q=1}^m \xi^p \eta^q \Delta\beta_{pq}^{m/c}, \quad \Phi_{\text{rec}}^m = \sum_{p+q=1}^M \xi^p \eta^q \sum_{i=1}^N \frac{1}{f^{p+q+i-1}} \Delta\beta_{pqi}^m \tag{4}$$

Here $(\xi = (x - x_c)/L_c, \eta = (y - y_c)/L_c)$ are scaled element-based local coordinates, where (x_c, y_c) are the centroidal coordinates of the element and L_c is a maximum element dimension. The scaling to (ξ, η) leads to an approximate range of variation $-1 \leq \xi \leq 1$ and $-1 \leq \eta \leq 1$ in most Voronoi cell elements, which avoids matrix ill-conditioning or poor invertability. The unknown coefficients $\Delta\beta^{m/c}$ associated with each term in the stress function expansions are evaluated in the FE solution process. The corresponding element stress increments in the matrix and inclusion phases are obtained from Equation (3) as

$$\{\Delta\boldsymbol{\sigma}^m\} = [\mathbf{P}^m]\{\Delta\boldsymbol{\beta}^m\}, \quad \{\Delta\boldsymbol{\sigma}^c\} = [\mathbf{P}^c]\{\Delta\boldsymbol{\beta}^c\} \tag{5}$$

Displacement increments on the Voronoi cell element boundary segments, as well as on segments of the matrix–inclusion interface are, respectively, interpolated as

$$\{\Delta \mathbf{u}\} = [\mathbf{L}^e]\{\Delta \mathbf{q}\}, \quad \{\Delta \mathbf{u}'\} = [\mathbf{L}^c]\{\Delta \mathbf{q}'\} \quad (6)$$

where $[\mathbf{L}^e]$ and $[\mathbf{L}^c]$ are interpolation matrices constructed from one-dimensional shape functions on the boundary segments. The weak form, matrix equations and solution methods of the VCFEM formulation have been discussed in detail in [47–49] and are not discussed in this paper.

2.2. Constitutive relations for the inclusion and matrix phases

The inclusion phase is assumed to be linear elastic, whereas the matrix phase is modeled using a rate-independent nonlocal GTN model [13, 23, 26]. The plastic part is modeled using an associated flow rule, where the evolving yield surface $\hat{\Phi} = 0$ is a function of the homogenized stress tensor σ_{ij} , and equivalent tensile flow stress representing the actual stress state in the matrix material σ_0 and the void volume fraction f as

$$\hat{\Phi} = \left(\frac{q}{\sigma_0}\right)^2 + 2f^*q_1 \cosh\left(-\frac{3q_2p}{2\sigma_0}\right) - (1 + q_3f^{*2}) = 0 \quad (7)$$

where q is the Von Mises stress $q = (\frac{3}{2}s_{ij}s_{ij})^{1/2}$ with $s_{ij} = \sigma_{ij} - \frac{1}{3}\sigma_{kk}\delta_{ij}$ the deviatoric stress, and $p = -\frac{1}{3}\sigma_{kk}$ is the hydrostatic pressure. q_1, q_2, q_3 are constants introduced by Tvergaard [54]. The acceleration function $f^*(f)$ has been introduced in [13] to model the complete loss of material stress-carrying capacity due to void coalescence as

$$f^* = \begin{cases} f, & f \leq f_c \\ f_c + \frac{f_u - f_c}{f_f - f_c}(f - f_c), & f > f_c \end{cases} \quad (8)$$

Here f_c is the critical void volume fraction at which void coalescence first occurs and f_f is the value at final failure. With increasing f^* , the effect of the hydrostatic stress on the plastic flow, and the GTN yield surface, becomes an ellipsoid in the stress space. Eventually as the void volume fraction $f \rightarrow f_f$, the acceleration function ($f^* \rightarrow f_u^* = 1/q_1$). At this value, the yield surface shrinks to a point manifesting loss of material load capacity corresponding to ductile failure. To avoid numerical difficulties, $f \rightarrow 0.95f_f$ is used instead of $f \rightarrow f_f$ in Equation (8). When $f = 0.95f_f$ at a given Gauss quadrature point, the void volume fraction is frozen at this value, implying local material failure. To avoid mesh sensitivity, a nonlocal evolution equation for the void volume fraction has been proposed in [23, 26, 55] incorporating a material length scale. The nonlocal void volume fraction growth rate at any material point $\bar{\mathbf{x}}$ is expressed as

$$\dot{f} = \frac{1}{W(\bar{\mathbf{x}})} \int_{\Omega_m} \dot{f}^{\text{local}}(\mathbf{x}) w(|\mathbf{x} - \bar{\mathbf{x}}|) d\Omega \quad (9)$$

where

$$W(\bar{\mathbf{x}}) = \int_{\Omega_m} w(|\mathbf{x} - \bar{\mathbf{x}}|) d\Omega \quad \text{and} \quad w(|\mathbf{x}|) = \left[\frac{1}{1 + (|\mathbf{x}|/L)^p} \right]^q$$

with $p=8, q=2$ and a material characteristic length, $MCL>0$. The weighting function $w(|\mathbf{x}|)=1$ at $|\mathbf{x}|=0$, $w(|\mathbf{x}|)=0.25$ at $|\mathbf{x}|=MCL$, and $w(|\mathbf{x}|)\rightarrow 0, \forall |\mathbf{x}|>MCL$ with a narrow transition region. The nonlocality is associated with spatial gradients in \dot{f} . The explicit introduction of the material length-scale parameter MCL regularizes the localization problem by preventing the matrix cracks from being unreasonably small.

In Equation (9) the local rate of change of the void volume fraction is due to growth of existing voids as well as due to nucleation of new voids, i.e.

$$\dot{f}^{local} = \dot{f}_{growth}^{local} + \dot{f}_{nucleation}^{local} \tag{10}$$

Owing to the plastic incompressibility of the matrix material, the void growth is

$$\dot{f}_{growth}^{local} = (1 - f)\dot{\bar{\epsilon}}_{kk}^p \tag{11}$$

Void nucleation is assumed to be by a plastic strain-controlled mechanism suggested by Chu and Needleman [22], and its rate is expressed in terms of the effective plastic strain in the matrix $\bar{\epsilon}_0^p$ as

$$\dot{f}_{nucleation}^{local} = A(\bar{\epsilon}_0^p)^{\dot{\bar{\epsilon}}_0^p} \tag{12}$$

where $A(\bar{\epsilon}_0^p)$ is a parameter that is generated using a normal distribution for nucleation parameter and is chosen as

$$A = \frac{f_N}{s_N\sqrt{2\pi}} \exp \left[-\frac{1}{2} \left(\frac{\bar{\epsilon}_0^p - \epsilon_N}{s_N} \right)^2 \right] \tag{13}$$

where ϵ_N is the mean strain for nucleation and s_N is its standard deviation; f_N is the volume fraction of void nucleating particles.

2.3. Strain update algorithm in VCFEM formulation

Stress update algorithm methods, proposed in, e.g. [56, 57] for the integration of the elasto-plastic constitutive equations in conjunction with displacement-based FE formulations, are not appropriate for the stress-based VCFEM formulation. In contrast, a new implicit strain update algorithm is used in this formulation. Ductile failure is preceded by strain softening, where the stress at a point decreases with additional straining, i.e. $\Delta\sigma$ is negative. The nonmonotonic stress behavior in VCFEM formulation is addressed through the use of the bisection method [58], a root-finding algorithm that repeatedly bisects an interval and then selects the subinterval in which the root exists, iIn particular, the *Regula Falsi* algorithm that retains the estimate for which the function value has an opposite sign from the function value at the current best estimate of the root. The increment in the void volume fraction Δf and the equivalent plastic strain increment in the matrix material $\Delta\bar{\epsilon}_0^p$ are used as line search parameters for generality.

The incremental update method discussed here is for the generalized plane strain case with a prescribed out-of-plane strain increment $\Delta\epsilon_{33}$ and in-plane stress increments $\Delta\sigma_{ij}, i, j=1, 2$. Three specific variables, namely increments of the void volume fraction Δf , effective matrix materials plastic strain $\Delta\bar{\epsilon}_0^p$ and the out-of-plane stress $\Delta\sigma_{33}$, are calculated in each increment. The three equations that should be solved for these variables are derived from the yield

condition, equivalence statement of plastic work and the plane strain condition, respectively, discussed next.

1. Effective yield condition $\hat{\Phi}=0$, for the homogenized porous material in Equation (7).
2. Equivalence of plastic work in the matrix material to that in homogenized porous material, i.e. $(1-f)\sigma_0\dot{\bar{\epsilon}}_0^p = \sigma_{ij}\dot{\epsilon}_{ij}^p = \dot{\lambda}\sigma_{ij}\partial\hat{\Phi}/\partial\sigma_{ij}$. The associated flow rule may be expressed in terms of the effective Von Mises stress q and the hydrostatic pressure p as

$$\dot{\epsilon}_{ij}^p = \dot{\lambda}\frac{\partial\hat{\Phi}}{\partial q}n_{ij} - \frac{1}{3}\dot{\lambda}\frac{\partial\hat{\Phi}}{\partial p}\delta_{ij} \quad \text{and} \quad \dot{\epsilon}_{kk}^p = -\dot{\lambda}\frac{\partial\hat{\Phi}}{\partial p} \tag{14}$$

where δ_{ij} is Kronecker's delta; $n_{ij} = \partial q / \partial \sigma_{ij}$. The incremental form of the plastic work equivalence then becomes

$$(1-f)\sigma_0\Delta\bar{\epsilon}_0^p = \sigma_{ij}\Delta\epsilon_{ij}^p = \Delta\lambda\frac{\partial\hat{\Phi}}{\partial p}p + \Delta\lambda\frac{\partial\hat{\Phi}}{\partial q}q \tag{15}$$

Combining Equations (10)–(12) with the second equation of (14) expresses the flow parameter $\Delta\lambda$ as

$$\Delta\lambda = \frac{\Delta f^{\text{local}} - A(\bar{\epsilon}_0^p)\Delta\bar{\epsilon}_0^p}{-(1-f)\partial\hat{\Phi}/\partial p} \tag{16}$$

Finally, substituting Equation (16) into Equation (15) results in a residual form of the equivalent plastic work:

$$R(\Delta\bar{\epsilon}_0^p, \Delta f^{\text{local}}, \Delta\sigma_{33}) = (1-f)\sigma_0\Delta\bar{\epsilon}_0^p + p\frac{\Delta f^{\text{local}} - A\Delta\bar{\epsilon}_0^p}{(1-f)} + 3q\frac{\Delta f^{\text{local}} - A\Delta\bar{\epsilon}_0^p}{(1-f)}\left(\frac{\partial\hat{\Phi}/\partial q}{\partial\hat{\Phi}/\partial p}\right) = 0 \tag{17}$$

With $\Delta\sigma_{ij}$ and Δf^{local} known, Equation (17) is used to determine the increment in plastic strain $\Delta\bar{\epsilon}_0^p$.

3. Generalized plane strain condition, with a specified out-of-plane normal strain increment, i.e.

$$\Delta\epsilon_{33} = \Delta\epsilon_{33}^e + \Delta\epsilon_{33}^p = \hat{\epsilon}^{\text{constant}} \tag{18}$$

Substituting the expression for $\Delta\epsilon_{33}$ from the generalized Hooke's law into Equation (18) yields the residual function in terms of $\Delta\sigma_{33}$, i.e.

$$G(\Delta\bar{\epsilon}_0^p, \Delta f^{\text{local}}, \Delta\sigma_{33}) = \frac{1}{E}(\Delta\sigma_{33} - \nu\Delta\sigma_{11} - \nu\Delta\sigma_{22}) + \Delta\lambda\left(-\frac{1}{3}\frac{\partial\hat{\Phi}}{\partial p} + \frac{3}{2q}\frac{\partial\hat{\Phi}}{\partial q}s_{33}\right) - \hat{\epsilon}^{\text{constant}} = 0 \tag{19}$$

The stress increment $\Delta\sigma_{33}$ can be evaluated from Equation (20), with $\Delta\sigma_{ij}$, $i, j = 1, 2$, Δf^{local} and $\Delta\bar{\epsilon}_0^p$ *a priori* known.

The above equations should be solved at each integration point of the element with known $\Delta\sigma_{ij}$ and matrix flow stress $\sigma_0(\bar{\epsilon}_0^p)$. The integration method, based on the Regula Falsi iteration algorithm, is summarized next.

1. **Initialize:** For iteration step $i = 1$, set $\Delta f^{\text{local}(i)} = 0$, $\Delta\bar{\epsilon}_0^{p(i)} = 0$ and $\Delta\sigma_{33}^i = 0$.
2. Evaluate $\hat{\Phi}$. If $\hat{\Phi} > 0$ then go to step 3 for the Regula Falsi scheme. Otherwise, go to step 2.3.
3. Start iteration with $\boxed{i = i + 1}$. The iteration will continue till the yield function $|\hat{\Phi}(\Delta f^{\text{local}(i-1)}, \Delta\bar{\epsilon}_0^{p(i-1)}, \Delta\sigma_{33}^{(i-1)})| \leq \text{Tolerance}_1$.
 - Set $\Delta f^{\text{local}(i)} = \Delta f^{\text{local}(i-1)}$, $\Delta\bar{\epsilon}_0^{p(i)} = \Delta\bar{\epsilon}_0^{p(i-1)}$ and $\Delta\sigma_{33}^i = \Delta\sigma_{33}^{(i-1)}$.
 - Keeping $\Delta\bar{\epsilon}_0^{p(i)}$ and $\Delta\sigma_{33}^i$ unchanged, assess two increments of void volume fraction ($\Delta f_1^{\text{local}(i)}$ and $\Delta f_2^{\text{local}(i)}$ ($\forall f \in [0, f_f]$)) such that

$$\hat{\Phi}_1(\Delta f_1^{\text{local}(i)}, \underbrace{\Delta\bar{\epsilon}_0^{p(i)}, \Delta\sigma_{33}^i}_{\text{Fixed}}) \times \hat{\Phi}_2(\Delta f_2^{\text{local}(i)}, \underbrace{\Delta\bar{\epsilon}_0^{p(i)}, \Delta\sigma_{33}^i}_{\text{Fixed}}) < 0$$

This corresponds to two opposite signs for the yield functions.

- Using the first of the two line searches as shown in Figure 2(a), obtain the incremental void volume fraction as the intercept on the $\hat{\Phi} = 0$ line, i.e.

$$\Delta f^{\text{local}(i)} = \Delta f_1^{\text{local}(i)} - \frac{\hat{\Phi}_1}{\hat{\Phi}_1 - \hat{\Phi}_2} (\Delta f_1^{\text{local}(i)} - \Delta f_2^{\text{local}(i)})$$

- Set $j = 1$, $\Delta\bar{\epsilon}_0^{p(j)} = \Delta\bar{\epsilon}_0^{p(i)}$ and $\Delta\sigma_{33}^j = \Delta\sigma_{33}^i$.
- For a given $\Delta f^{\text{local}(i)}$, start iteration with $\boxed{j = j + 1}$. The iteration will continue as long as the plastic work equation $|R(\Delta f^{\text{local}(i)}, \Delta\bar{\epsilon}_0^{p(j-1)}, \Delta\sigma_{33}^{j-1})| > \text{Tolerance}_2$.
- Set $\Delta\bar{\epsilon}_0^{p(j)} = \Delta\bar{\epsilon}_0^{p(j-1)}$ and $\Delta\sigma_{33}^j = \Delta\sigma_{33}^{(j-1)}$.
 - For the known value of $\Delta f^{\text{local}(i)}$, assess two increments of effective plastic strain ($\Delta\bar{\epsilon}_{0(1)}^{p(j)}$ and $\Delta\bar{\epsilon}_{0(2)}^{p(j)}$) such that

$$R_1(\Delta f^{\text{local}(i)}, \Delta\bar{\epsilon}_{0(1)}^{p(j)}, \Delta\sigma_{33}^j) \times R_2(\Delta f^{\text{local}(i)}, \Delta\bar{\epsilon}_{0(2)}^{p(j)}, \Delta\sigma_{33}^j) < 0$$

- Use the second of the two line searches as shown in Figure 2(b) and obtain the incremental effective plastic strain as the intercept on the $R = 0$ line, i.e.

$$\Delta\bar{\epsilon}_0^{p(j)} = \Delta\bar{\epsilon}_{0(1)}^{p(j)} - \frac{R_1}{R_1 - R_2} (\Delta\bar{\epsilon}_{0(1)}^{p(j)} - \Delta\bar{\epsilon}_{0(2)}^{p(j)})$$

- Set $k = 1$, $\Delta\sigma_{33}^k = \Delta\sigma_{33}^j$.

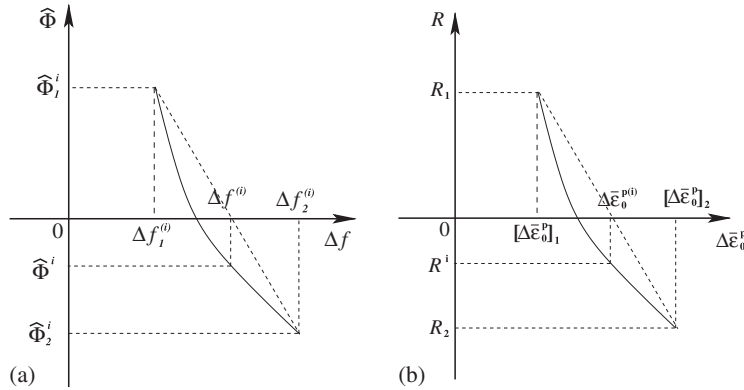


Figure 2. Line search in the Regula Falsi algorithm for (a) yield function $\hat{\Phi}(\Delta f^{\text{local}})$ and (b) equivalent plastic work $R(\Delta \bar{\epsilon}_0^p(i))$.

- o With $\Delta f^{\text{local}(i)}$ and $\Delta \bar{\epsilon}_0^p(j)$ known from the previous steps, start iteration with $k = k + 1$. The iteration will continue as long as the residual function of generalized plane strain condition in Equation (19) $|G(\Delta f^{\text{local}(i)}, \Delta \bar{\epsilon}_0^p(j), \Delta \sigma_{33}^{(k-1)})| > \text{Tolerance}_3$.

— Use the Newton–Raphson method iteration method to determine $\Delta \sigma_{33}^k$ as

$$\Delta \sigma_{33}^k = \Delta \sigma_{33}^{(k-1)} - \frac{G(\Delta f^{\text{local}(i)}, \Delta \bar{\epsilon}_{0(1)}^p(j), \Delta \sigma_{33}^{(k-1)})}{(\partial G / \partial \Delta \sigma_{33})(\Delta f^{\text{local}(i)}, \Delta \bar{\epsilon}_{0(1)}^p(j), \Delta \sigma_{33}^{(k-1)})}$$

- o Set $\Delta \sigma_{33}^j = \Delta \sigma_{33}^k$ and update

$$R_1 = R(\Delta f^{\text{local}(i)}, \Delta \bar{\epsilon}_0^p(j), \Delta \sigma_{33}^j), \quad \Delta \bar{\epsilon}_{0(1)}^p(j) = \Delta \bar{\epsilon}_0^p(j) \quad \text{if } R > 0$$

$$R_2 = R(\Delta f^{\text{local}(i)}, \Delta \bar{\epsilon}_0^p(j), \Delta \sigma_{33}^j), \quad \Delta \bar{\epsilon}_{0(2)}^p(j) = \Delta \bar{\epsilon}_0^p(j) \quad \text{if } R < 0$$

- Set $\Delta \bar{\epsilon}_0^p(i) = \Delta \bar{\epsilon}_0^p(j)$, $\Delta \sigma_{33}^i = \Delta \sigma_{33}^j$ and update

$$\hat{\Phi}_1 = \hat{\Phi}(\Delta f^{\text{local}(i)}, \Delta \bar{\epsilon}_0^p(i), \Delta \sigma_{33}^i), \quad \Delta f_1^{\text{local}(i)} = \Delta f^{\text{local}(i)} \quad \text{if } \hat{\Phi} > 0$$

$$\hat{\Phi}_2 = \hat{\Phi}(\Delta f^{\text{local}(i)}, \Delta \bar{\epsilon}_0^p(i), \Delta \sigma_{33}^i), \quad \Delta f_2^{\text{local}(i)} = \Delta f^{\text{local}(i)} \quad \text{if } \hat{\Phi} < 0$$

4. Calculate $\Delta \epsilon_{ij}^e$ from the elasticity relations, $\Delta \epsilon_{ij}^p$ from the associated flow rule (14) and $\Delta \epsilon_{ij}$ by adding the two.

An implicit backward Euler time integration scheme is used in the numerical implementation of the stress-based VCFEM. It requires an iterative solution process in which tangent operators are obtained through linearized forms of constitutive equations. Solving the linearized element equations requires evaluation of the instantaneous linearized compliance tensor, defined as the

variation of total strain caused by the variation of the stress. These are evaluated at the end of the step between n and $n+1$ as

$$S_{ijkl} = \left. \frac{d\varepsilon_{ij}}{d\sigma_{kl}} \right|_{(n+1)}$$

The method introduced in [56] is used to compute $S_{ijkl} = D_{ijkl}^{-1}$, where D_{ijkl} is the stiffness matrix. It requires the evaluation of $\Delta\varepsilon_p = -\Delta\lambda(\partial\Phi/\partial p)|_{(n+1)}$, $\Delta\varepsilon_q = \Delta\lambda(\partial\Phi/\partial q)|_{(n+1)}$ from Equation (14) with known values of Δf , $\Delta\bar{\varepsilon}_0^p$ and $\Delta\varepsilon_{33}$ and the flow parameter $\Delta\lambda$ from Equation (16).

2.4. Aspects of numerical implementation

Various aspects of numerical implementation of algorithms in VCFEM have been discussed in [47] and are not addressed here. These include proper conditioning of element-level matrices to ensure their invertability, choice on the number of stress parameters $\Delta\beta^m$ and $\Delta\beta^c$ to avoid rank insufficiencies and suppression of rigid body modes in the deformation field of the interface for enhancing the accuracy and convergence of the VCFEM solutions. Another important issue is the numerical integration, which is performed by subdividing the matrix domain Ω_m and the inclusion domain Ω_c into quadrilaterals and triangles, respectively, and applying quadrature formula for corresponding domains. To account for the effect of the high gradients in the stress functions due to the reciprocal terms in Equation (4), a graded discretization is induced in the matrix domain near the interface. Details of the integration procedure are provided in [59].

Finally, an adaptive methodology developed in [47] to enhance convergence characteristics and accuracy of the VCFEM for analyzing heterogeneous material response is implemented in this paper. Nodal DOFs on the element boundary and interface and stress interpolation functions are, respectively, enriched based on two local error measures. The first is a traction reciprocity error, which is derived *a posteriori* from the element and interface traction discontinuity in the solution. This error indicator is used to enhance displacement DOFs. The second is a strain energy error, which may be related to the error in kinematic relation. This error indicator is used to enrich stress interpolations.

2.5. Validation tests of the VCFEM for porous plasticity without inclusion or matrix cracking

Validation of the VCFEM for the porous plastic heterogeneous materials is done through two sets of examples. The first set compares VCFEM results with those generated by the commercial code ABAQUS and evaluates VCFEM convergence rates, whereas the second example compares with experimental results for checking the stress in particles of actual microstructure. Only small strain kinematics are considered in these examples.

2.5.1. Comparison with ABAQUS and convergence test. The VCFEM results for a local GTN model without void coalescence are compared with those generated by ABAQUS commercial code for the small strain problem shown in Figure 3 with an inclusion volume fraction $V_f = 20\%$. As shown in Figure 3(a), at $x=0$, all DOFs in the Y -direction are constrained to remain zero, whereas DOFs in the X -direction are constrained to be zero at $y=0$. Periodicity conditions are enforced on the surface $y=L$ by constraining it to remain horizontal and straight. The analysis is conducted under plane strain conditions. The RVEs are loaded in uniaxial tension to a macroscopic tension

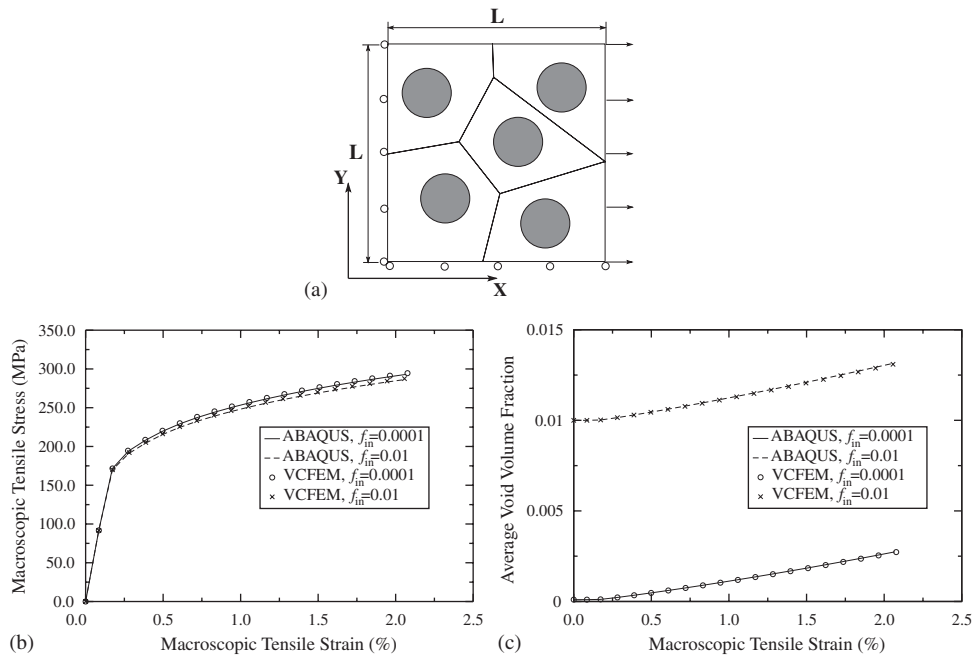


Figure 3. (a) A square domain with five circular inclusions and the corresponding Voronoi cell mesh, the comparison of (b) volume-averaged stress–strain response and (c) average void volume fraction evolution.

strain $\bar{\varepsilon}_{x,x} = 2.0\%$. The matrix material is assumed to be a ductile Al–3.5% Cu alloy with elastic–plastic material properties: Young’s modulus $E = 72$ GPa; the Poisson ratio $\nu = 0.32$; post yield behavior $\sigma_m = \sigma_0(\varepsilon_m^p/\varepsilon_0 + 1)^N$, with $\sigma_0 = 175$ MPa and $N = 0.2$. Here $\varepsilon_0 = \sigma_0/E$ is the uniaxial strain at yield. The inclusion is SiC with elastic properties: Young’s modulus $E = 450$ GPa and the Poisson ratio $\nu = 0.17$. Void nucleation parameters are chosen as $\varepsilon_N = 0.1$, $s_N = 0.1$ and $f_N = 0.04$. The problem is solved with two values of initial void volume fraction, namely $f_{in} = 0.0001$ and $f_{in} = 0.01$. Each element in the VCFEM model of Figure 3(a) has 12 nodes on element boundary and 8 nodes on matrix–inclusion interface. The inclusion stress function is generated using 33 polynomial terms (seventh-order polynomial stress function). The matrix stress function has an additional 36 reciprocal terms due to the inclusion shape (three reciprocal terms for each polynomial exponent from 2 to 4, i.e. $i = p + q \dots p + q + 2$, $\forall p + q = 2 \dots 4$). The ABAQUS mesh has 37 828 bilinear QUAD-4 elements.

The volume-averaged stress–strain response and the average void volume fraction–strain are plotted in Figures 3(b) and (c), respectively. Excellent match is observed in these results with the two approaches. The efficiency of VCFEM in comparison with ABAQUS is demonstrated in Table I. On an IBM System Cluster 1350 with single 2.66 HZ AMD Opteron processor, the VCFEM simulations are approximately 200% faster than the ABAQUS simulations. This efficiency increases further with the number of inclusions.

The convergence rate of the VCFEM results is examined with respect to the (i) *average traction reciprocity error* (ATRE) and (ii) *average strain energy error* (ASEE) discussed in [47]. The starting values of the stress and nodal displacement DOFs are mentioned above. The total DOFs

Table I. Comparison of simulation times by the two approaches.

	ABAQUS simulations (s)	VCFEM simulations (s)
With $f_{in} = 0.0001$	233	132
With $f_{in} = 0.01$	237	134

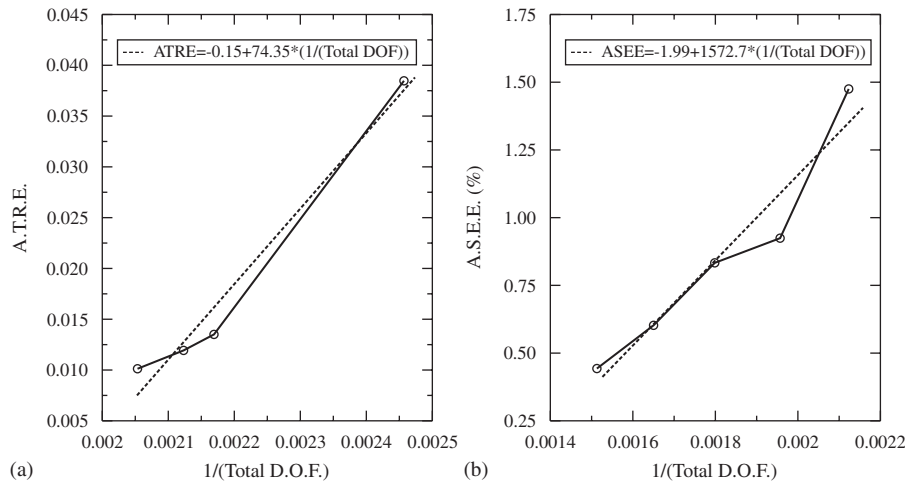


Figure 4. VCFEM convergence rate: (a) average traction reciprocity error (ATRE) and (b) average strain energy error (ASEE), plotted as functions of the total degrees of freedom.

correspond to the sum of the total displacement DOFs at the interface and element boundary and the number of β parameters, i.e. $DOF = 2 \times N_{nodes} + N_{\beta}$. Figure 4 plots the *ATRE* and *ASEE* as functions of the inverse of DOF. A maximum *ATRE* change of 65% results from a 13% increase in DOF. The *ASEE* drops from 1.48 to 0.44% by enriching the polynomial terms of stress function in each element from sixth order to 10th order. The high accuracy of VCFEM is confirmed by the near linear convergence rates.

2.5.2. Comparison of inclusion stresses obtained by Raman spectroscopy. In this example, experimentally extracted stresses in Si particles of a cast aluminum alloy A356-T6 microstructure are compared with VCFEM simulations. A micrograph of the cast alloy is shown in Figure 5(a). As shown in Figure 5(b), the sample is loaded in the y -direction by an applied strain. Loading direction stresses on the surface of the water are experimentally evaluated by micro-Raman spectroscopy executed by Harris *et al.* [60, 61]. Two eutectic Si particles are singled out for interrogation. Residual stresses due to heat treatment are subtracted from the experimentally acquired data shown in Figure 6. The particle stresses increase linearly at the initial stages of loading due to elastic deformation. However, the stress increments reduce substantially with straining after matrix yield with ensuing plastic deformation in the matrix.

For the VCFEM simulation, the aluminum matrix is an elastic–plastic material with properties $E = 72 \text{ GPa}$, $\nu = 0.33$, and the post yield behavior is represented by Ramberg–Osgood law

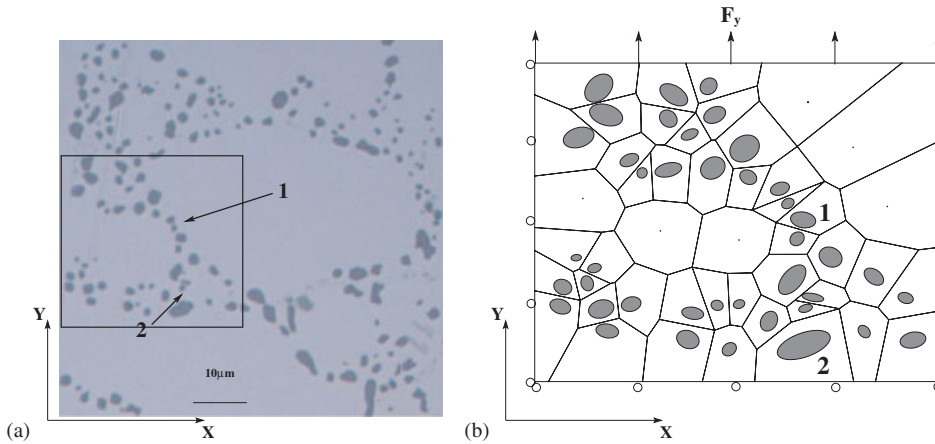


Figure 5. (a) A micrograph of cast aluminum alloy A356-T6 showing Si particles interrogated for stresses by Raman spectroscopy and (b) the VCFEM model of a part of the microstructure.

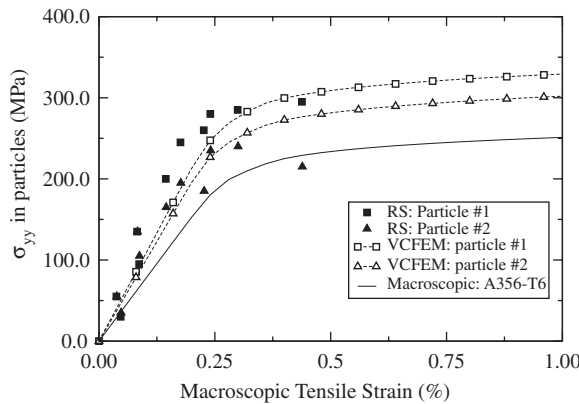


Figure 6. Comparison of volume-averaged stresses $\bar{\sigma}_{yy}$ in the two Si particles as a function of the macroscopic applied strain by VCFEM simulation with those by Raman spectroscopy.

($\sigma_m = \sigma_0(\epsilon_m^p / \alpha \epsilon_0)^{1/n}$). The initial flow stress of matrix $\sigma_0 = 200$ MPa, $\epsilon_0 = \sigma_0 / E$, $\alpha = 3/7$ and the strain hardening exponent $n = 17.5$. The Si particles are linear elastic with properties $E = 170$ GPa, $\nu = 0.17$. The simulation is conducted with plane strain assumptions. Figure 6 compares the simulated stresses with the experimental stresses. The VCFEM results concur with the experimental results. Table II also compares the slope $\Delta\sigma_{yy} / \Delta\epsilon_{yy}$, where $\Delta\sigma_{yy}$ is the average particle stress and $\Delta\epsilon_{yy}$ is the average strain in the specimen. The stress in particle #1 is larger than that in particle #2. The corresponding values of NND in the table indicate that larger particle stresses occur with smaller NND. Hence, stresses in clustered regions can be significantly higher for the same size of particles.

Table II. Stress–strain slope $\Delta\sigma_{yy}/\Delta\varepsilon_{yy}$ in the elastic regime.

	Experimental results (Pa)	VCFEM results (Pa)	Nearest-neighbor distance (μm)
Particle #1	118430	106848	0.44
Particle #2	90000	98218	1.55
Average	104215	102533	

3. VCFEM FOR INCLUSION CRACKING IN A POROUS PLASTIC MATRIX

The VCFEM has been successfully applied to the simulation of brittle cracking of inclusions contained in ductile matrix materials in [3, 51]. As shown in Figure 1, each Voronoi cell element now consists of a crack phase Ω_{cr} in addition to the matrix phase Ω_m and the inclusion phase Ω_e . Instantaneous splitting of an inclusion is assumed once a crack initiation criterion is satisfied at a point in the inclusion. Initiation is assumed to be triggered by a Weibull-statistics-based extension of the Beremin model [62], which incorporates the local principal stresses as well as the inclusion size. In this criterion, the probability of fracture F_{fr} for a particle of volume v is

$$F_{fr} = 1 - \exp \left[-\frac{v}{v_0} \left(\frac{\sigma_1^c}{\sigma_w} \right)^m \right] \quad (20)$$

where m and σ_w are the Weibull modulus and the characteristic strength, respectively, v_0 is a reference volume, and σ_1^c is the maximum principal stress at a point in an inclusion. Once F_{fr} reaches a predetermined critical value $F_{critical}$ at an integration point, an elliptical crack phase with a high aspect ratio $a/b=10$ is introduced in the inclusion. In the computational procedure, more than one point may satisfy the fracture criterion during increment. Consequently, the location of the crack is determined by a weighted averaging method as

$$x_{crack} = \sum x \frac{\sigma_1^c(x, y)}{\sigma_w} / \sum \frac{\sigma_1^c(x, y)}{\sigma_w}, \quad y_{crack} = \sum y \frac{\sigma_1^c(x, y)}{\sigma_w} / \sum \frac{\sigma_1^c(x, y)}{\sigma_w} \quad \forall [F_{fr} > F_{critical}] \quad (21)$$

The orientation of the major axis of the elliptical crack is normal to the principal stress directions at (x_{crack}, y_{crack}) .

In addition to the element displacement and stress fields in Section 2.1, the displacement field \mathbf{u}'' on the crack boundary $\partial\Omega_{cr}$ is now a solution variable: the VCFEM formulation. The energy functional (1) is modified to accommodate the inclusion crack phase as

$$\begin{aligned} \Pi_e^{IC}(\Delta\boldsymbol{\sigma}^m, \Delta\boldsymbol{\sigma}^c, \Delta\mathbf{u}, \Delta\mathbf{u}', \Delta\mathbf{u}'') &= \Pi_e^{ND}(\Delta\boldsymbol{\sigma}^m, \Delta\boldsymbol{\sigma}^c, \Delta\mathbf{u}, \Delta\mathbf{u}') \\ &\quad - \int_{\partial\Omega_{cr}} (\boldsymbol{\sigma}^c + \Delta\boldsymbol{\sigma}^c) \cdot \mathbf{n}^{cr} \cdot (\mathbf{u}'' + \Delta\mathbf{u}'') \, d\partial\Omega \end{aligned} \quad (22)$$

and the domain energy functional is $\Pi^{IC} = \sum_{e=1}^N \Pi_e^{IC}$. The superscript ‘cr’ corresponds to variables on the crack boundary and \mathbf{n}^{cr} the outward normal on the crack face. With the addition of the extra crack phase in a Voronoi cell element, stress functions and their associated stress fields are automatically adjusted to account for the altered topology. The crack boundary $\partial\Omega_{cr}$ is parametrical as a function $f_{cr}(x, y) = 1$ through a conformal mapping technique. Again f_{cr} exhibits the property

$f_{cr} \rightarrow \infty$ as $(x, y) \rightarrow \infty$. The corresponding stress functions in Equation (3) are automatically updated for the matrix and particle phases as

$$\Phi^m = \Phi_{poly}^m + \Phi_{rec}^m + \Phi_{rec}^{cm}, \quad \Phi^c = \Phi_{poly}^c + \Phi_{rec}^{cc} \quad (23)$$

Additionally, the displacement field $\Delta \mathbf{u}''$ is interpolated from the corresponding values $\{\Delta \mathbf{q}''\}$ at the nodes on the crack surface as

$$\{\Delta \mathbf{u}''\} = [\mathbf{L}^{cr}] \{\Delta \mathbf{q}''\} \quad (24)$$

Here $[\mathbf{L}^{cr}]$ is taken as a quadratic interpolation matrix. The weak form and the solution procedure are discussed in detail in [3, 51].

3.1. Numerical example on inclusion cracking

This study develops a method for calibrating Weibull parameters governing inclusion cracking and subsequently compares VCFEM simulations with experimental results. The cracking criterion in Equation (20) is modified to yield the volume fraction of fractured inclusions, corresponding to a known distribution $p(v)$ of the inclusion size in the microstructure as

$$\rho(V) = \int_{V_{min}}^{V_{max}} p(v) F_{fr} dv \approx \sum_{i=1}^N p(v_i) \left(1 - \exp \left[-\frac{v_i}{v_0} \left(\frac{\sigma_I^i}{\sigma_w} \right)^m \right] \right) \Delta v_i \quad (25)$$

where V_{min} and V_{max} delineate the range of particle volumes. The probability density $p(v_i)$ of particle volume v_i (area in two dimensions) can be obtained from experimental micrographs. The entire range of particle volumes is divided into N intervals, such that for the i th interval $\Delta v_i = v_i - v_{i-1}$ ($i = 1, 2, \dots, N$). σ_I^i is the average maximum principal stress in inclusions with sizes in the range of $[v_{i-1}, v_i]$.

Micrographs of two sections of an Aluminum alloy W319-T7 are used to calibrate the Weibull parameters σ_w and m . One of the micrographs of dimension $81.2 \mu\text{m} \times 81.2 \mu\text{m}$ and the corresponding VCFE model are shown in Figures 7(a) and (b). The matrix phase is aluminum and the inclusion phase is eutectic silicon particles in this alloy. In addition, there is a small volume fraction of brittle, copper-based intermetallics. A histogram of the number fraction of the particle area in micrograph #1 is shown in Figure 7(c). The particle area fraction (VF), total number of particles (NP) and total number of cracked particles (NCP) at a strain $\varepsilon_{yy} = 6.21\%$ for the two sections are tabulated in Table III.

VCFEM simulations of the equivalent microstructures, e.g. of Figures 7(b), are conducted to evaluate the maximum principal stress in particles that have experimentally cracked at a known strain. The silicon particles are modeled with the linear elastic properties $E_{Si} = 170 \text{ GPa}$, $\nu_{Si} = 0.17$, whereas the intermetallics have the elastic properties $E_{In} = 128 \text{ GPa}$, $\nu_{In} = 0.36$. The aluminum matrix material is modeled as porous material with properties $E_{Al} = 72 \text{ GPa}$, $\nu_{Al} = 0.33$, and the post yield behavior is represented by Ramberg–Osgood law ($\sigma_m = \sigma_0 (\varepsilon_m^p / \alpha \varepsilon_0)^{1/n}$). The initial flow stress of matrix $\sigma_0 = 200 \text{ MPa}$, $\varepsilon_0 = \sigma_0 / E$, $\alpha = \frac{3}{7}$ and the strain hardening exponent $n = 17.5$. The initial void volume fraction is assumed to be zero. The Weibull parameter m is assumed to be the same for the Si particles and the intermetallics. However, the parameter σ_w in these inclusion materials is assumed to vary in the same ratio as their respective Young's modulus, i.e. $(\sigma_w)_{Si} / E_{Si} = (\sigma_w)_{In} / E_{In}$. The material is subjected to a tensile total strain of $\varepsilon_{yy} = 6.21\%$. All simulations are conducted under plane strain condition.

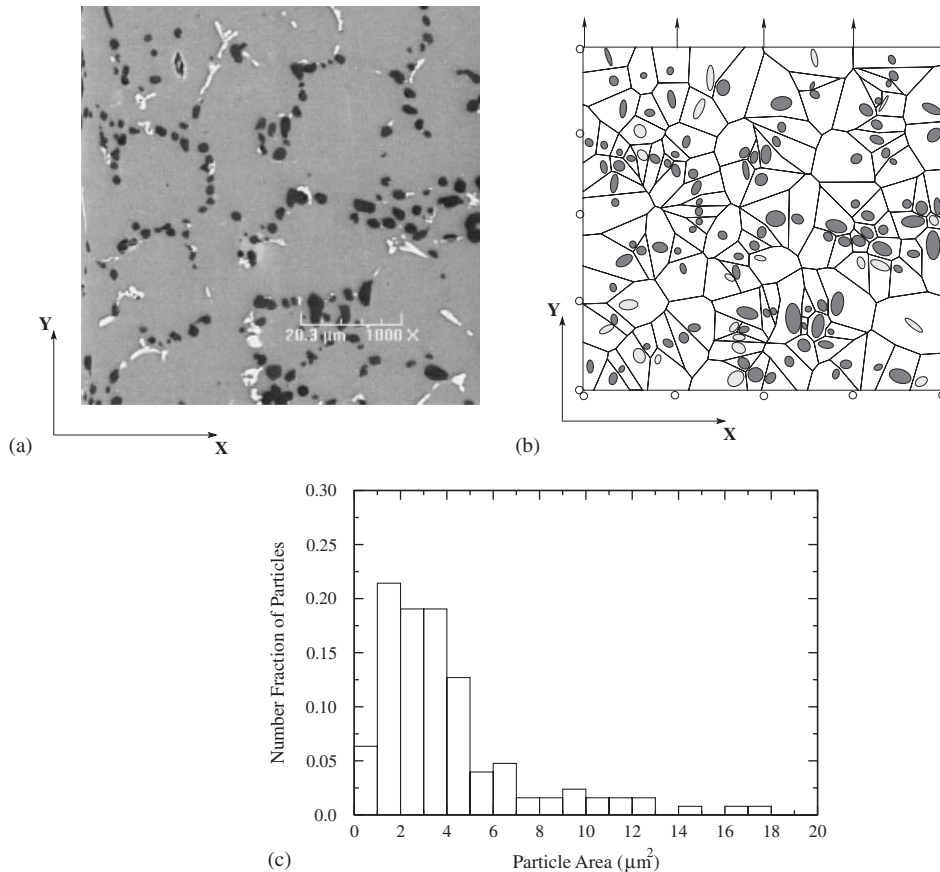


Figure 7. (a) Scanning electron micrograph of section #1 of W319-T7 aluminum alloy (dark ellipses are Si particles and white ellipses are copper-based intermetallics); (b) corresponding VCFEM mesh and model; and (c) histogram of the number fraction of particle area for section.

Different values of the Weibull parameters $(\sigma_w)_{Si}$ are calibrated corresponding to a range of values of m between 1 and 8 and are tabulated in Table IV. Figure 8(a) shows the probability density of damaged particles for the section micrograph #1 simulated with different values of m . The simulations show that generally good match with experiments is obtained with m between 2 and 3, and a value $m=2.4$ is selected for subsequent analyses. The parameter (σ_w) is calibrated from results of VCFEM simulations prior to particle cracking. The number of cracked particles resulting from VCFEM simulations with different values of σ_w is shown in Table V. The Weibull parameters that yield maximum agreement with experiments are $m=2.4$ and $(\sigma_w)_{Si}=0.68$ GPa. The distribution of the fraction of damaged particles as a function of the particle size is shown in Figure 8(b). The comparison with experimentally observed plots shows similar trends with a small phase shift. This may be attributed to the difference between the two-dimensional simulations and three-dimensional experimental observations. Figure 9 shows the contour plots of the effective plastic strain at $\varepsilon_{yy}=6.21\%$ without matrix cracking.

Table III. Experimentally observed (i) particle volume fraction (VF), (ii) total number of particles (NP) and (iii) total number of cracked particles (NCP) for the two micrographs of W319-T7 at a total strain $\varepsilon_{yy} = 6.21\%$.

Micrograph #	VF (%)	NP	NCP
1	9.18	129	34
2	7.86	101	19

Table IV. Weibull parameters $(\sigma_w)_{Si}$ calibrated from VCFEM simulations.

m	1	2	2.4	3	4	5	6	7	8
$(\sigma_w)_{mic\#1}$ (GPa)	0.355	0.555	0.600	0.652	0.700	0.750	0.780	0.812	0.825
$(\sigma_w)_{mic\#2}$ (GPa)	0.400	0.615	0.650	0.700	0.776	0.812	0.855	0.870	0.900

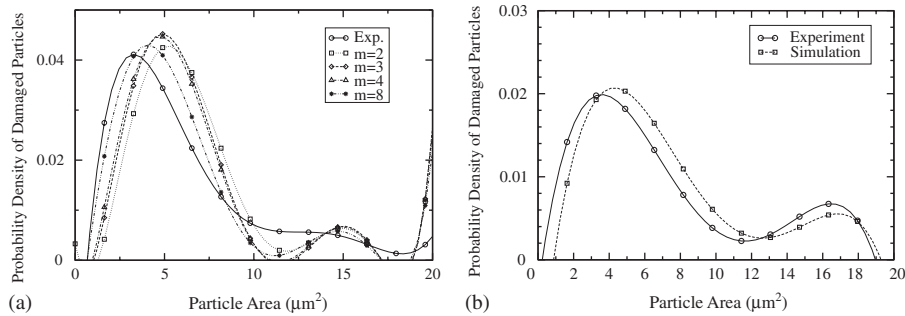


Figure 8. Experimental and simulated probability densities of cracked particle volumes with different Weibull moduli m and (b) distribution of number fraction of damaged particles as functions of particle size for micrograph 1 with $m=2.4$ and $(\sigma_w)_{Si}=0.68$ GPa.

Table V. Number of cracked particles in experiments and by VCFEM simulation using different values of σ_w .

Micrograph #	Exp.	$\sigma_w=0.625$	$\sigma_w=0.635$	$\sigma_w=0.65$	$\sigma_w=0.66$	$\sigma_w=0.67$	$\sigma_w=0.68$
1	34	47	35	35	33	32	32
2	19	31	25	23	23	24	21

4. LOCALLY ENHANCED VCFEM FOR MATRIX CRACKING

In ductile fracture, inclusion cracking is often followed by localization in ligaments of intense void evolution that results in a transition of the local stress–strain response from hardening to the softening behavior with a negative stiffness. The assumed stress-based VCFEM formulation, discussed in the previous sections, faces numerical instabilities in this regime due to nonuniqueness in strains or boundary displacements for given values of stresses. Two strain values may correspond

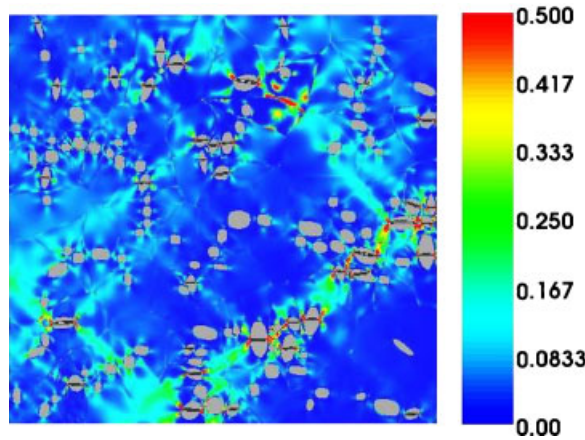


Figure 9. Contour plots of effective plastic strain for micrograph 1.

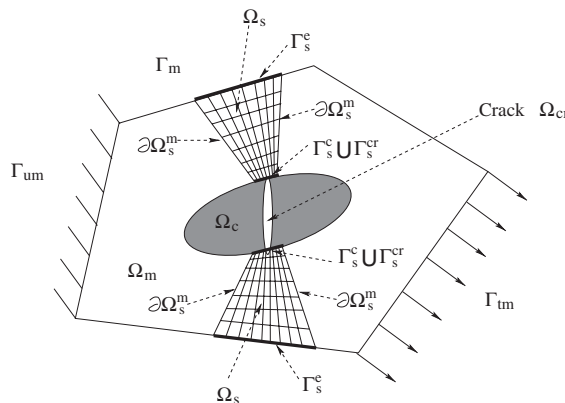


Figure 10. A locally enhanced Voronoi cell element with superposed displacement-based elements.

to a given value of stress in the stress–strain response curve. This can cause problems with convergence, especially near the peak corresponding to the onset of softening. To avert such instabilities and also to provide a high resolution to the strain localization zone, regions of strain softening Ω_s are adaptively augmented with a patch of high-resolution displacement-based finite elements within each Voronoi cell element. A typical locally enhanced VCFEM (LE-VCFE) is shown in Figure 10. A finite deformation formulation for the elasto-porous plasticity governs the behavior of displacement-based elements in Ω_s .

A typical locally enhanced Voronoi cell element (LE-VCE) may consist of four phases: the matrix phase Ω_m , the inclusion phase Ω_c , the inclusion crack phase Ω_{cr} and a matrix region of localized strain softening Ω_s preceding ductile failure. $\partial\Omega_s$ is the boundary Ω_s with an outward normal \mathbf{n}^s . $\partial\Omega_s$ may consist of four distinct regions, depending on its overlap with pre-existing topological regions in the Voronoi cell element, i.e. $\partial\Omega_s = \Gamma_s^e \cup \Gamma_s^c \cup \Gamma_s^{cr} \cup \partial\Omega_s^m$. Here $\Gamma_s^e = \partial\Omega_e \cap \partial\Omega_s$, $\Gamma_s^c = \partial\Omega_c \cap \partial\Omega_s$ and $\Gamma_s^{cr} = \partial\Omega_{cr} \cap \partial\Omega_s$ represent the intersections of $\partial\Omega_s$ with the element, inclusion and crack

boundaries, respectively. The aggregate of these common boundaries is represented as $\Gamma_s = \Gamma_s^e \cup \Gamma_s^c \cup \Gamma_s^{cr}$. Once the displacement-based local FE region Ω_s is overlaid, a variable mapping procedure described in [63] is used to map local stresses, strains and material internal variables from the Voronoi cells element domain Ω_e to displacement elements in Ω_s . Superscript s labels variables associated with Ω_s . The mapping should guarantee displacement compatibility on the shared boundaries Γ_s between the stress and displacement interpolated regions as shown in Figure 10, i.e.

$$\mathbf{u}^s = \mathbf{u} \text{ on } \Gamma_s^e, \quad \mathbf{u}^s = \mathbf{u}' \text{ on } \Gamma_s^c, \quad \mathbf{u}^s = \mathbf{u}'' \text{ on } \Gamma_s^{cr} \tag{26}$$

Here \mathbf{u} , \mathbf{u}' and \mathbf{u}'' are the displacement DOFs on the boundaries $\partial\Omega_e$, $\partial\Omega_c$ and $\partial\Omega_{cr}$, respectively.

4.1. Criteria for local enhancement

The increased void growth rate in the vicinity of inclusion crack tips leads to void coalescence, which is associated with a post-peak strain softening. Beyond this peak or bifurcation point, the solution becomes unstable with the stress-based VCFEM formulation. The Regula Falsi integration algorithm for the GTN model in Section 2.3 does not converge. Correspondingly, a local transition criterion is devised for introducing displacement interpolated elements $\Omega_s \in \Omega_e$, stated as

$$\Omega_e \rightarrow \Omega_e \setminus \Omega_s \cup \Omega_s \text{ if } \frac{\partial q}{\partial \bar{\epsilon}^p} \leq 0 \text{ and } \bar{\epsilon}^p \geq \bar{\epsilon}_{critical}^p \tag{27}$$

where q is the Von Mises stress $q = (\frac{3}{2} s_{ij} s_{ij})^{1/2}$ and $\bar{\epsilon}^p$ is the effective plastic strain at an integration point. In the computational procedure, the enhanced region is opened if at least five neighboring integration points meet criterion (27). Ω_s is set larger than the actual region at which strain softening occurs to ensure that deformation on its boundary $\partial\Omega_s$ conforms to that of the small strain region $\Omega_e \setminus \Omega_s$ at their common interface. Frequent enhancement during the ductile fracture process is also avoided by this larger region.

4.2. Constitutive relations and stress update algorithm

A finite deformation formulation is developed for elements in Ω_s following the framework developed in [64]. The constitutive relations in Ω_s are described in a rotated Lagrangian system in terms of the rotated Cauchy stress tensor $\boldsymbol{\sigma}_R^s = \mathbf{R}^T \boldsymbol{\sigma}^s \mathbf{R}$ and the incremental rotated strain tensor $\Delta \boldsymbol{\epsilon}_R^s = \mathbf{R}^T \Delta \boldsymbol{\epsilon}^s \mathbf{R}$ [65]. Here \mathbf{R} is a proper orthogonal tensor representing pure rotation obtained from the polar decomposition of the deformation gradient tensor $\mathbf{F}^s = \nabla_0 \mathbf{x}^s$. The GTN constitutive model in Ω_s is integrated using the unconditionally stable backward Euler algorithm presented in [56]. In the $(n + 1)$ th increment between deformed configurations Ω_s^n and Ω_s^{n+1} the rotated Cauchy stress is updated as

$$(\boldsymbol{\sigma}_R^s)^{n+1} = (\boldsymbol{\sigma}_R^s)^n + (\mathbf{D}_R^{ep})^{n+1} : (\Delta \boldsymbol{\epsilon}_R^s)^{n+1} \tag{28}$$

where $(\mathbf{D}_R^{ep})_{ijkl}^{n+1} = (\partial(\boldsymbol{\sigma}_R^s)_{ij} / \partial(\boldsymbol{\epsilon}_R^s)_{kl})|_{n+1}$ is the elastic–plastic tangent stiffness tensor in the rotated configuration at the end of the $(n + 1)$ th increment. The integration algorithm in [56] solves the following set of non-linear equations in the rotated Lagrangian coordinates.

$$\text{Yield function: } \hat{\Phi}(p, q, f, \Delta \bar{\epsilon}^p) = \left(\frac{q}{\sigma_0}\right)^2 + 2f^* q_1 \cosh\left(-\frac{3q_2 p}{2\sigma_0}\right) - (1 + q_3 f^{*2}) = 0 \tag{29}$$

$$\text{Flow equation: } \Delta \epsilon_p \frac{\partial \hat{\Phi}}{\partial q} + \Delta \epsilon_q \frac{\partial \hat{\Phi}}{\partial p} = 0 \tag{30}$$

where $p = p^e + K \Delta \varepsilon_p$ and $q = q^e - 3G \Delta \varepsilon_q$ are the hydrostatic stress and the equivalent stress, respectively. $\Delta \varepsilon_p = -\Delta \Lambda \partial \hat{\Phi} / \partial p$ and $\Delta \varepsilon_q = \Delta \Lambda \partial \hat{\Phi} / \partial q$ are the primary unknowns in the above equations. The additional variables in the above equations are defined in terms of $\Delta \varepsilon_p$ and $\Delta \varepsilon_q$ as

$$\Delta \bar{\varepsilon}^p = \frac{-p \Delta \varepsilon_p + q \Delta \varepsilon_q}{(1-f)\sigma_0}, \quad \Delta f = (1-f)\Delta \varepsilon_p + A \Delta \bar{\varepsilon}^p \tag{31}$$

where σ_0 and A are functions of the microscopic equivalent plastic strain $\bar{\varepsilon}^p$. These equations are solved iteratively using the Newton–Raphson method with a known incremental strain tensor $\Delta(\varepsilon_{ij}^s)^{n+1} = \partial(\Delta u_i^s)^{n+1} / \partial x_j^{n+1}$. Here $\Delta \mathbf{u}^{(n+1)}$ corresponds to the displacement increments in the $(n+1)$ th increment. The rotated strain increment is expressed as

$$(\Delta(\varepsilon_{ij})_R^s)^{n+1} = R_{ki}^{n+1} \Delta(\varepsilon_{kl}^s)^{n+1} R_{lj}^{n+1} \tag{32}$$

Equations (29) and (30) are solved iteratively for $\Delta \varepsilon_p$ and $\Delta \varepsilon_q$ till their corrections have reached a prescribed tolerance. The rotated stress is calculated from the hydrostatic and deviatoric components p^{n+1} and q^{n+1} , after which the updated Cauchy stress in Ω_s^{n+1} and the corresponding increment are obtained using the tensor rotation formula.

4.3. Coupling stress and displacement interpolated regions in LE-VCFEM formulation

With the addition of displacement elements in Ω_s , the energy functional in Equations (22) should be augmented for the LE-VCFEM formulation. It couples small deformation assumed stress formulation in $\Omega_e \setminus \Omega_s$ with the finite deformation formulation in displacement elements of Ω_s . For Ω_s , all variables are referred to the current configuration. The corresponding incremental element energy functional Π_e^{MC} for $(n+1)$ th increment is defined in terms of stresses, boundary and interface displacement fields, and internal displacements as

$$\begin{aligned} \Pi_e^{MC}(\Delta \boldsymbol{\sigma}^m, \Delta \boldsymbol{\sigma}^c, \Delta \mathbf{u}, \Delta \mathbf{u}', \Delta \mathbf{u}'', \Delta \mathbf{u}^s) = & \Pi_e^{IC} - \int_{\Omega_s} \Delta A(\Delta \boldsymbol{\sigma}^s, \Delta \boldsymbol{\varepsilon}^s) d\Omega - \int_{\Omega_s} \boldsymbol{\sigma}^s : \Delta \boldsymbol{\varepsilon}^s d\Omega \\ & + \int_{\partial \Omega_s = \Gamma_s \cup \partial \Omega_s^m} (\boldsymbol{\sigma}^m + \Delta \boldsymbol{\sigma}^m) \cdot \mathbf{n}^s \cdot (\mathbf{u}^s + \Delta \mathbf{u}^s) d\partial \Omega \end{aligned} \tag{33}$$

where $\Delta A (= \frac{1}{2} \Delta \sigma_{ij}^s \Delta \varepsilon_{ij}^s)$ is the incremental strain energy density and $\Delta \sigma_{ij}^s$ and $\Delta \varepsilon_{ij}^s$ are the stress and strain increments. The total energy functional for the domain is $\Pi^{MC} = \sum_{e=1}^N \Pi_e^{MC}$. The first variational of Π_e^{MC} in Equation (33) is expressed as

$$\begin{aligned} \delta \Pi_e^{MC}(\Delta \boldsymbol{\sigma}^m, \Delta \boldsymbol{\sigma}^c, \Delta \mathbf{u}, \Delta \mathbf{u}', \Delta \mathbf{u}'', \Delta \mathbf{u}^s) = & - \int_{\Omega_m} \Delta \boldsymbol{\varepsilon}^m : \delta \Delta \boldsymbol{\sigma}^m d\Omega - \int_{\Omega_m} \boldsymbol{\varepsilon}^m : \delta \Delta \boldsymbol{\sigma}^m d\Omega \\ & - \int_{\Omega_c} \Delta \boldsymbol{\varepsilon}^c : \delta \Delta \boldsymbol{\sigma}^c d\Omega - \int_{\Omega_c} \boldsymbol{\varepsilon}^c : \delta \Delta \boldsymbol{\sigma}^c d\Omega + \int_{\partial \Omega_e} \delta \Delta \boldsymbol{\sigma}^m \cdot \mathbf{n}^e \cdot (\mathbf{u} + \Delta \mathbf{u}) d\partial \Omega \\ & + \int_{\partial \Omega_e} (\boldsymbol{\sigma}^m + \Delta \boldsymbol{\sigma}^m) \cdot \mathbf{n}^e \cdot \delta \Delta \mathbf{u} d\partial \Omega - \int_{\Gamma_{tm}} (\bar{\mathbf{t}} + \Delta \bar{\mathbf{t}}) \cdot \delta \Delta \mathbf{u} d\Gamma \end{aligned}$$

$$\begin{aligned}
 & - \int_{\partial\Omega_c} (\delta\Delta\boldsymbol{\sigma}^m - \delta\Delta\boldsymbol{\sigma}^c) \cdot \mathbf{n}^c \cdot (\mathbf{u}' + \Delta\mathbf{u}') \, d\partial\Omega \\
 & - \int_{\partial\Omega_c} (\boldsymbol{\sigma}^m + \Delta\boldsymbol{\sigma}^m - \boldsymbol{\sigma}^c - \Delta\boldsymbol{\sigma}^c) \cdot \mathbf{n}^c \cdot \delta\Delta\mathbf{u}' \, d\partial\Omega - \int_{\partial\Omega_{cr}} \delta\Delta\boldsymbol{\sigma}^c \cdot \mathbf{n}^{cr} \cdot (\mathbf{u}'' + \Delta\mathbf{u}'') \, d\partial\Omega \\
 & - \int_{\partial\Omega_{cr}} (\boldsymbol{\sigma}^c + \Delta\boldsymbol{\sigma}^c) \cdot \mathbf{n}^{cr} \cdot \delta\Delta\mathbf{u}'' \, d\partial\Omega - \boxed{\int_{\Omega_s} (\boldsymbol{\sigma}^s + \Delta\boldsymbol{\sigma}^s) : \nabla \delta\Delta\mathbf{u}^s \, d\Omega} \\
 & + \boxed{\int_{\Gamma_s \cup \partial\Omega_s^m} \delta\Delta\boldsymbol{\sigma}^m \cdot \mathbf{n}^s \cdot (\mathbf{u}^s + \Delta\mathbf{u}^s) \, d\partial\Omega + \int_{\Gamma_s \cup \partial\Omega_s^m} (\boldsymbol{\sigma}^m + \Delta\boldsymbol{\sigma}^m) \cdot \mathbf{n}^s \cdot \delta\Delta\mathbf{u}^s \, d\partial\Omega} \tag{34}
 \end{aligned}$$

Applying divergence theorem to the first of the boxed terms yields

$$\int_{\Omega_s} (\boldsymbol{\sigma}^s + \Delta\boldsymbol{\sigma}^s) : \nabla \delta\Delta\mathbf{u}^s \, d\Omega = - \int_{\Omega_s} \nabla \cdot (\boldsymbol{\sigma}^s + \Delta\boldsymbol{\sigma}^s) \cdot \delta\Delta\mathbf{u}^s \, d\Omega + \int_{\Gamma_s \cup \partial\Omega_s^m} (\boldsymbol{\sigma}^s + \Delta\boldsymbol{\sigma}^s) \cdot \mathbf{n}^s \cdot \delta\Delta\mathbf{u}^s \, d\partial\Omega \tag{35}$$

Setting the first variation of Π with respect to the incremental displacement field $\Delta\mathbf{u}^s$ and incremental stress field $\Delta\boldsymbol{\sigma}$ on the subdomain boundary $\Gamma_s \cup \partial\Omega_s^m$ to zero, respectively, yields the following Euler equations:

$$\text{Equilibrium: } \nabla \cdot (\boldsymbol{\sigma}^s + \Delta\boldsymbol{\sigma}^s) = 0 \quad \text{in } \Omega_s \tag{36}$$

$$\text{Traction reciprocity: } (\boldsymbol{\sigma} + \Delta\boldsymbol{\sigma}) \cdot \mathbf{n}^s = (\boldsymbol{\sigma}^s + \Delta\boldsymbol{\sigma}^s) \cdot \mathbf{n}^s \quad \text{on } \Gamma_s \cup \partial\Omega_s^m \tag{37}$$

$$\text{Element boundary displacement continuity: } \mathbf{u}^s + \Delta\mathbf{u}^s = \mathbf{u} + \Delta\mathbf{u} \quad \text{on } \Gamma_s^e \tag{38}$$

$$\text{Interface displacement continuity: } \mathbf{u}^s + \Delta\mathbf{u}^s = \mathbf{u}' + \Delta\mathbf{u}' \quad \text{on } \Gamma_s^c \tag{39}$$

$$\text{Crack face displacement continuity: } \mathbf{u}^s + \Delta\mathbf{u}^s = \mathbf{u}'' + \Delta\mathbf{u}'' \quad \text{on } \Gamma_s^{cr} \tag{40}$$

The increments of stress $\Delta\boldsymbol{\sigma}^s$ in the above equations are obtained from the rotated Cauchy stresses. Deformation in Ω_s is governed by the weak forms of the traction and displacement boundary conditions in Equations (37)–(40). Displacement compatibility between the stress and displacement interpolated regions is satisfied in a weak sense, as shown in the Euler equations (38)–(40). Additionally, traction reciprocity is satisfied in a weak sense on the boundary $\partial\Omega_s^m$ between the two domains.

4.4. Weak form and matrix assembly

The displacement increments $\{\Delta\mathbf{u}^s\}$ in the last three terms of Equation (34) for each element in the enhanced region Ω_s are interpolated as

$$\{\Delta\mathbf{u}^s\} = \{\mathbf{N}^s\}^T \{\Delta\mathbf{q}_e^s\} \tag{41}$$

Within each Voronoi cell element, the region Ω_s may consist of several displacement-based elements. Nine-noded quadrilateral elements are used in Ω_s with Lagrangian shape functions \mathbf{N}^s . Let the union of all the element nodal displacements be represented as the generalized displacement field $\{\Delta\mathbf{q}^s\} = \bigcup \{\Delta\mathbf{q}_e^s\}$. Furthermore, the generalized displacement field may be subdivided into two groups; one corresponding to nodes on the boundary $\partial\Omega_s$ and the other corresponding to nodes

in the interior $\Omega_s \setminus \partial\Omega_s$, i.e. $\Delta\mathbf{q}^s = \Delta\mathbf{q}_1^s \cup \Delta\mathbf{q}_2^s$, where $\Delta\mathbf{q}_1^s$ corresponds to $\partial\Omega_s$ and $\Delta\mathbf{q}_2^s$ belongs to $\Omega_s \setminus \partial\Omega_s$. To avoid duplicity, $\Delta\mathbf{q}$, $\Delta\mathbf{q}'$ and $\Delta\mathbf{q}''$ will henceforth correspond to displacement fields in the respective boundary domains that do not overlap with $\partial\Omega_s$.

Setting the first variation of the energy functional (33) with respect to the stress coefficients $\Delta\beta^m$ and $\Delta\beta^c$, respectively, to zero results in the weak forms of the kinematic relations as

$$\begin{aligned} \int_{\Omega_m} [\mathbf{P}^m]^T \{\boldsymbol{\varepsilon}^m + \Delta\boldsymbol{\varepsilon}^m\} d\Omega &= \int_{\partial\Omega_e} [\mathbf{P}^m]^T [\mathbf{n}^e]^T [\mathbf{L}^e] \{\Delta\mathbf{q}\} d\partial\Omega \\ &\quad - \int_{\partial\Omega_c} [\mathbf{P}^m]^T [\mathbf{n}^c]^T [\mathbf{L}^c] \{\Delta\mathbf{q}'\} d\partial\Omega \\ &\quad - \boxed{\int_{\Gamma_s^e \cup \partial\Omega_s^m} [\mathbf{P}^m]^T [\mathbf{n}^s]^T [\mathbf{N}^s] \{\Delta\mathbf{q}_1^s\} d\partial\Omega} \end{aligned} \tag{42}$$

and

$$\begin{aligned} \int_{\Omega_c} [\mathbf{P}^c]^T \{\boldsymbol{\varepsilon}^c + \Delta\boldsymbol{\varepsilon}^c\} d\Omega &= \int_{\partial\Omega_c} [\mathbf{P}^c]^T [\mathbf{n}^c]^T [\mathbf{L}^c] \{\Delta\mathbf{q}'\} d\partial\Omega \\ &\quad - \int_{\partial\Omega_{cr}} [\mathbf{P}^c]^T [\mathbf{n}^{cr}]^T [\mathbf{L}^{cr}] \{\Delta\mathbf{q}''\} d\partial\Omega \\ &\quad - \boxed{\int_{\Gamma_s^c \cup \Gamma_s^{cr}} [\mathbf{P}^c]^T [\mathbf{n}^s]^T [\mathbf{N}^s] \{\Delta\mathbf{q}_1^s\} d\partial\Omega} \end{aligned} \tag{43}$$

The boxed terms highlight the addition due to the locally enhanced region Ω_s . Next, for the displacement elements in Ω_s , the variational statement for the principle of virtual work may be expressed by setting the coefficients of $\delta\Delta\mathbf{u}^s$ to zero as

$$\delta\Pi_s(\Delta\mathbf{u}^s) = - \int_{\Omega_s} (\boldsymbol{\sigma}^m + \Delta\boldsymbol{\sigma}^m) : \nabla\delta(\Delta\mathbf{u}^s) d\Omega + \int_{\partial\Omega_s} (\boldsymbol{\sigma} + \Delta\boldsymbol{\sigma}) \cdot \mathbf{n}^s \cdot \delta(\Delta\mathbf{u}^s) d\partial\Omega = 0 \tag{44}$$

The traction $\boldsymbol{\sigma} \cdot \mathbf{n}^s$ on the boundary $\partial\Omega_s$ is imposed from the stresses in the region $\Omega_m \setminus \Omega_s$ on Ω_s . In an incremental solution method, the principle of virtual work and hence all variables in Equation (44) are expressed in the $n+1$ th configuration Ω_s^{n+1} . Substituting the displacement interpolation equation (41) in Equation (44) and noting that $\delta(\Delta\mathbf{q}^s)$ is arbitrary lead to the equation that should be solved for the $(n+1)$ th increment:

$$\begin{aligned} \int_{\Omega_s^{n+1}} [\bar{\mathbf{B}}]^T \{\boldsymbol{\sigma}^s\}^{n+1} d\Omega &= \int_{(\Gamma_s^e)^{n+1} \cup (\partial\Omega_s^m)^{n+1}} [\mathbf{N}^s]^T [\mathbf{n}^s]^T [\mathbf{P}^m] \{\boldsymbol{\beta}^m + \Delta\boldsymbol{\beta}^m\} d\partial\Omega \\ &\quad + \int_{(\Gamma_s^c)^{n+1} \cup (\Gamma_s^{cr})^{n+1}} [\mathbf{N}^s]^T [\mathbf{n}^s]^T [\mathbf{P}^c] \{\boldsymbol{\beta}^c + \Delta\boldsymbol{\beta}^c\} d\partial\Omega \end{aligned} \tag{45}$$

where $[\bar{\mathbf{B}}]$ is the strain–displacement matrix using selective reduced integration to prevent volumetric locking [66]. Consequently, in the solution process, the iterative correction $\{d\mathbf{q}^s\}^i$ to the displacement solution $\{\Delta\mathbf{q}^s\}^i$ is solved from

$$[\mathbf{K}_s]^i \{d\mathbf{q}^s\}^i = \{\mathbf{F}_s\}^i \tag{46}$$

where

$$\begin{aligned}
 [\mathbf{K}_s]^i &= \int_{\Omega_s^{n+1}} [\bar{\mathbf{B}}]^T [\mathbf{D}^{ep}]^i [\bar{\mathbf{B}}] d\Omega \\
 \{\mathbf{F}_s\}^i &= \int_{(\Gamma_s^e)^{n+1} \cup (\partial\Omega_s^m)^{n+1}} [\mathbf{N}^s]^T [\mathbf{n}^s]^T [\mathbf{P}^m] \{\boldsymbol{\beta}^m + \Delta\boldsymbol{\beta}^m\}^i d\partial\Omega \\
 &\quad + \int_{(\Gamma_s^c)^{n+1} \cup (\Gamma_s^{cr})^{n+1}} [\mathbf{N}^s]^T [\mathbf{n}^s]^T [\mathbf{P}^c] \{\boldsymbol{\beta}^c + \Delta\boldsymbol{\beta}^c\}^i d\partial\Omega - \int_{\Omega_s^{n+1}} [\bar{\mathbf{B}}] (\{\boldsymbol{\sigma}^s\}^{n+1})^i d\Omega
 \end{aligned} \tag{47}$$

Here $[\mathbf{D}^{ep}]^i$ is the elasto-plastic tangent stiffness matrix in the i th iteration. For coupling equations (46) in Ω_s with those in the VCFEM formulation, the displacement decomposition $\Delta\mathbf{q}^s = \Delta\mathbf{q}_1^s \cup \Delta\mathbf{q}_2^s$ mentioned earlier is necessary, in (46) i.e.

$$d\mathbf{q}^s = \begin{Bmatrix} d\mathbf{q}_1^s \\ d\mathbf{q}_2^s \end{Bmatrix} \Rightarrow \begin{bmatrix} \mathbf{K}_{11}^s & \mathbf{K}_{12}^s \\ \mathbf{K}_{22}^s & \mathbf{K}_{22}^s \end{bmatrix}^i \begin{Bmatrix} d\mathbf{q}_1^s \\ d\mathbf{q}_2^s \end{Bmatrix}^i = \begin{Bmatrix} \mathbf{F}_1^s \\ \mathbf{F}_2^s \end{Bmatrix}^i \tag{48}$$

Using static condensation, Equation (48) may be re-written as

$$([\mathbf{K}_{11}^s] - [\mathbf{K}_{12}^s][\mathbf{K}_{22}^s]^{-1}[\mathbf{K}_{21}^s])\{d\mathbf{q}_1^s\} = \{\mathbf{F}_1^s\} - [\mathbf{K}_{12}^s][\mathbf{K}_{22}^s]^{-1}\{\mathbf{F}_2^s\} \tag{49}$$

Finally, setting the first variation of the total energy functional Π with respect to $\Delta\mathbf{q}$, $\Delta\mathbf{q}'$, $\Delta\mathbf{q}''$ and $\Delta\mathbf{q}_1^s$ to zero results in the weak form of the traction reciprocity conditions:

$$\sum_{e=1}^N \begin{bmatrix} \int_{\partial\Omega_e} [\mathbf{L}^e]^T [\mathbf{n}^e]^T [\mathbf{P}^m] d\partial\Omega & \mathbf{0} \\ -\int_{\partial\Omega_e} [\mathbf{L}^c]^T [\mathbf{n}^e]^T [\mathbf{P}^m] d\partial\Omega & \int_{\partial\Omega_e} [\mathbf{L}^c]^T [\mathbf{n}^c]^T [\mathbf{P}^c] d\partial\Omega \\ \mathbf{0} & \int_{\partial\Omega_{cr}} [\mathbf{L}^{cr}]^T [\mathbf{n}^{cr}]^T [\mathbf{P}^c] d\partial\Omega \\ \int_{\Gamma_s^e \cup \partial\Omega_s^m} [\mathbf{N}^s]^T [\mathbf{n}^s]^T [\mathbf{P}^m] d\partial\Omega & \int_{\Gamma_s^c \cup \Gamma_s^{cr}} [\mathbf{N}^s]^T [\mathbf{n}^s]^T [\mathbf{P}^c] d\partial\Omega \end{bmatrix} \begin{Bmatrix} \boldsymbol{\beta}^m + \Delta\boldsymbol{\beta}^m \\ \boldsymbol{\beta}^c + \Delta\boldsymbol{\beta}^c \end{Bmatrix} \\
 = \sum_{e=1}^N \begin{bmatrix} \int_{\Gamma_{tm}} [\mathbf{L}^e]^T \{\bar{\mathbf{t}} + \Delta\bar{\mathbf{t}}\} d\Omega \\ \mathbf{0} \\ \mathbf{0} \\ \int_{\partial\Omega_s} [\mathbf{N}^s]^T [\mathbf{n}^s]^T \{\boldsymbol{\sigma}^s\} d\partial\Omega \end{bmatrix} \tag{50}$$

In the iterative solution process, let $\{\Delta\boldsymbol{\beta}\}^i$ correspond to a linearized correction of $\{\Delta\boldsymbol{\beta}\}^i$'s in the i th iteration, i.e.

$$\begin{Bmatrix} \Delta\boldsymbol{\beta}^m \\ \Delta\boldsymbol{\beta}^c \end{Bmatrix} = \begin{Bmatrix} \Delta\boldsymbol{\beta}^m \\ \Delta\boldsymbol{\beta}^c \end{Bmatrix}^i + \begin{Bmatrix} d\boldsymbol{\beta}^m \\ d\boldsymbol{\beta}^c \end{Bmatrix}^i \tag{51}$$

The elemental equations in the i th iteration step are then obtained by substituting Equation (51) into Equations (42) and (43) to yield

$$\begin{bmatrix} \mathbf{H}_m & \mathbf{0} \\ \mathbf{0} & \mathbf{H}_c \end{bmatrix} \begin{Bmatrix} d\boldsymbol{\beta}^m \\ d\boldsymbol{\beta}^c \end{Bmatrix}^i = \begin{bmatrix} \mathbf{G}_e & -\mathbf{G}_{cm} & \mathbf{0} & \mathbf{G}_{sm} \\ \mathbf{0} & \mathbf{G}_{cc} & -\mathbf{G}_{cr} & \mathbf{G}_{sc} \end{bmatrix}^i \begin{Bmatrix} \Delta \mathbf{q} \\ \Delta \mathbf{q}' \\ \Delta \mathbf{q}'' \\ \Delta \mathbf{q}_1^s \end{Bmatrix}^i - \begin{Bmatrix} \int_{\Omega_m \setminus \Omega_s} [\mathbf{P}^m]^T \{\boldsymbol{\varepsilon} + \Delta \boldsymbol{\varepsilon}\} d\Omega \\ \int_{\Omega_c} [\mathbf{P}^c]^T \{\boldsymbol{\varepsilon} + \Delta \boldsymbol{\varepsilon}\} d\Omega \end{Bmatrix}^i \quad (52)$$

where

$$\begin{aligned} [\mathbf{H}_m] &= \int_{\Omega_m \setminus \Omega_s} [\mathbf{P}^m]^T [\mathbf{S}^m] [\mathbf{P}^m] d\Omega, & [\mathbf{H}_c] &= \int_{\Omega_c} [\mathbf{P}^c]^T [\mathbf{S}^c] [\mathbf{P}^c] d\Omega \\ [\mathbf{G}_e] &= \int_{\partial\Omega_e} [\mathbf{P}^m]^T [\mathbf{n}^e] [\mathbf{L}^e] d\partial\Omega, & [\mathbf{G}_{cm}] &= \int_{\partial\Omega_c} [\mathbf{P}^m]^T [\mathbf{n}^e] [\mathbf{L}^c] d\partial\Omega \\ [\mathbf{G}_{cc}] &= \int_{\partial\Omega_c} [\mathbf{P}^c]^T [\mathbf{n}^c] [\mathbf{L}^c] d\partial\Omega \end{aligned} \quad (53)$$

and $[\mathbf{S}]$ is the tangent compliance matrix in each phase. Additionally,

$$[\mathbf{G}_{sm}] = \int_{\Gamma_s^e \cup \partial\Omega_s^m} [\mathbf{P}^m]^T [\mathbf{n}^s]^T [\mathbf{N}^s] d\partial\Omega \quad \text{and} \quad [\mathbf{G}_{sc}] = \int_{\Gamma_s^c \cup \Gamma_s^{\text{cr}}} [\mathbf{P}^c]^T [\mathbf{n}^s]^T [\mathbf{N}^s] d\partial\Omega \quad (54)$$

The iterative solver of Equation (50) sets up the following equation in the j th iteration step:

$$\sum_{e=1}^N [[\mathbf{G}]^T [\mathbf{H}]^T [\mathbf{G}]^i] \begin{Bmatrix} d\mathbf{q} \\ d\mathbf{q}' \\ d\mathbf{q}'' \\ d\mathbf{q}_1^s \end{Bmatrix}^j = \sum_{e=1}^N \begin{Bmatrix} \int_{\Gamma_m} [\mathbf{L}^e]^T \{\bar{\mathbf{t}} + \Delta \bar{\mathbf{t}}\} d\partial\Omega \\ \mathbf{0} \\ \mathbf{0} \\ \int_{\partial\Omega_s} [\mathbf{N}^s]^T [\mathbf{n}^s]^T \{\boldsymbol{\sigma}^s\} d\partial\Omega \end{Bmatrix} - \sum_{e=1}^N \begin{Bmatrix} \int_{\partial\Omega_e} [\mathbf{L}^e]^T [\mathbf{n}^e]^T [\mathbf{P}^m] d\partial\Omega \\ - \int_{\partial\Omega_e} [\mathbf{L}^c]^T [\mathbf{n}^c]^T [\mathbf{P}^m] d\partial\Omega \\ \mathbf{0} \\ \int_{\Gamma_s^e \cup \partial\Omega_s^m} [\mathbf{N}^s]^T [\mathbf{n}^s]^T [\mathbf{P}^m] d\partial\Omega \end{Bmatrix} - \begin{Bmatrix} \mathbf{0} \\ \int_{\partial\Omega_c} [\mathbf{L}^c]^T [\mathbf{n}^c]^T [\mathbf{P}^c] d\partial\Omega \\ \int_{\partial\Omega_{\text{cr}}} [\mathbf{L}^{\text{cr}}]^T [\mathbf{n}^{\text{cr}}]^T [\mathbf{P}^c] d\partial\Omega \\ \int_{\Gamma_s^c \cup \Gamma_s^{\text{cr}}} [\mathbf{N}^s]^T [\mathbf{n}^s]^T [\mathbf{P}^c] d\partial\Omega \end{Bmatrix} \begin{Bmatrix} \boldsymbol{\beta}^m + d\boldsymbol{\beta}^m \\ \boldsymbol{\beta}^c + d\boldsymbol{\beta}^c \end{Bmatrix} \quad (55)$$

the interface of the two domains. Elements to be refined are determined from a criterion based on the gradient of void volume fraction:

$$\text{Refine element E, if: } \|\nabla f\| \geq g_{\text{crit}} \text{ at an integration point} \quad (61)$$

The value of g_{crit} is set to $0.5(f_c - f_{\text{in}})/l_{\text{in}}$, where f_c is the critical void volume fraction for coalescence, f_{in} is the initial void volume fraction and l_{in} is the distance to the closest integration point.

5. NUMERICAL EXAMPLES OF DUCTILE FRACTURE WITH LE-VCFEM

The locally enhanced VCFE model (LE-VCFEM) is used for simulating ductile fracture of materials containing a dispersion of brittle inclusions. Three different problems are considered. The first study conducts a sensitivity analysis of ductile fracture with respect to various geometric configurations. The second study investigates the effect of evolving void volume fraction in the elasto-plastic matrix constitutive equations on ductile fracture. In the final study, ductile fracture of a real microstructure is simulated. In the first two studies, the matrix is assumed to be a ductile porous material with elastic-plastic behavior, while the inclusion is brittle with elastic properties. The post yield behavior of the ductile matrix is characterized by the relation $\sigma_m = \sigma_0(\epsilon_m^p/\epsilon_0 + 1)^N$. Material parameters are $E_m = 72.0 \text{ GPa}$, $\nu_m = 0.32$, $E_i = 427.0 \text{ GPa}$, $\nu_i = 0.17$, $\sigma_0 = 340.0 \text{ MPa}$ and $N = 0.2$.

5.1. Sensitivity analysis with respect to spatial distribution of inclusions

Four different microstructures, (A), (B), (C) and (D), shown in Figure 11, are used to investigate the effect of spatial distribution of inclusions. The different spatial distributions considered are uniform square edge-packed, uniform square diagonal-packed, hard-core random and hard-core with clustering, respectively. All inclusions are of the same size. Microstructures (A), (C) and (D) have an inclusion volume fraction $V_f = 15\%$, whereas (B) has a volume fraction $V_f = 13.8\%$. Table VI lists a few important characterization functions, namely *NND*, *Cluster index* and *Contour index*. The *NND* corresponds to the minimum surface-to-surface distance between two particles. *Cluster index* and *Contour index* are quantities that characterize the level of clustering and have been defined in [69]. *Cluster index* quantifies the intensity of packing in a cluster represented by the number of inclusions in a prescribed region, whereas *Contour index* accounts for the area fraction of inclusions within the same region. The distribution of *NND* for microstructures (C) and (D) is plotted in Figure 12 showing the higher peak at lower *NND* for microstructure (D).

LE-VCFEM simulations are conducted with the void and particle crack nucleation parameters $\epsilon_N = 0.2$, $s_N = 0.075$, $f_N = 0.08$, $\sigma_w = 0.5 \text{ GPa}$ and $m = 2.4$ in the GTN and Weibull models, respectively. Porosity parameters $f_{\text{in}} = 0.001$ and the material characteristic length, $\text{MCL} = 0.09L$ are used. For each Voronoi cell element, stress functions and boundary displacement field interpolations are shown in Table VII. The table depicts the order of stress functions, number of terms in the stresses, number of displacement DOFs on $\partial\Omega_c$ and the maximum number of displacement DOFs on $\partial\Omega_e$, respectively. The eighth-order polynomial stress functions correspond to 42 stress terms and the 36 reciprocal terms are due to three reciprocal terms for each polynomial exponent from 2 to 4, i.e. $i = p + q \dots p + q + 2$, $\forall p + q = 2 \dots 4$. After particle cracking, another 36 reciprocal terms are added into the stress function for both matrix and inclusion.

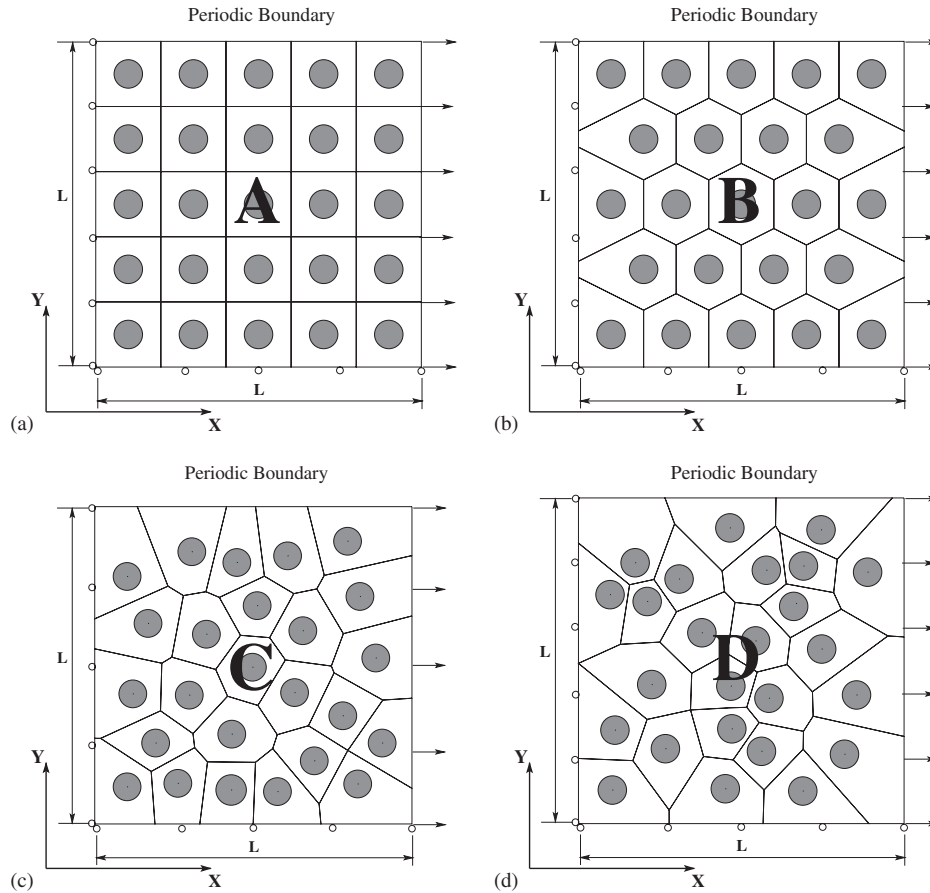


Figure 11. Four different microstructures with their Voronoi cell meshes: (a) uniform square edge-packed; (b) uniform square diagonal-packed; (c) hard-core random; and (d) hard-core with clustering.

Table VI. Microstructural characterization functions.

Microstructure	Max. NND	Min. NND	Avg. NND	Cluster index	Contour index
(A)	0.1126	0.1126	0.1126	2.2157	0.2204
(B)	0.1126	0.1126	0.1126	1.8187	0.2987
(C)	0.1132	0.0545	0.0726	2.7525	0.5702
(D)	0.1060	0.0275	0.0589	3.4049	0.6739

Note: All the dimensions are in fractions of size L of the microstructure.

Plane strain simulations are conducted with symmetry conditions on the edges $x=0$ and $y=0$ through zero displacement boundary conditions in Figure 11. The top boundary $y=L$ is constrained to remain horizontal and a prescribed displacement is applied to the boundary $x=L$ along the

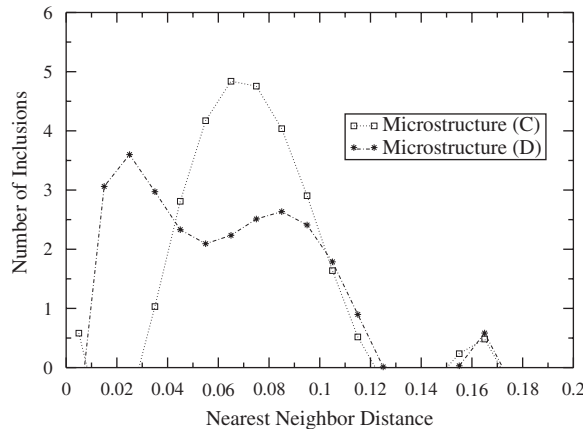


Figure 12. Distribution of nearest-neighbor distance (NND) for microstructures (C) and (D).

Table VII. Stress-related parameters and pre-enhancement displacement degrees of freedom in each Voronoi cell element.

$O(\Phi_{poly}^m)$	σ_{poly}^m terms	σ_{rec}^m terms	$O(\Phi_{poly}^c)$	σ_{poly}^c terms	$\partial\Omega_c$ DOF	$\partial\Omega_e$ DOF
8	42	36	8	42	16	32

x -direction, representing an applied strain ϵ_{xx} . The Voronoi cell model for the microstructure with the locally enhanced displacement elements at the final strain is shown in Figure 13. Figure 14 shows the macroscopic stress–strain response with a depiction of the strain to failure and ductility. Furthermore, the strains to failure for each microstructure are listed in Table VIII. The uniformly distributed square microstructure (A) has the highest ductility and fracture resistance, whereas the clustered microstructure (D) with more inclusions at smaller NNDs has the worst fracture properties. Higher local stresses at smaller NNDs cause inclusions to crack early. This initiates ductile fracture in the matrix, which accelerates localization of damage to cause catastrophic failure.

Figure 15 shows contour plots of the void volume fraction f at the final stage of straining. For (A) all the inclusions crack at the same time because of the uniform distribution and f evolves simultaneously. The final fracture path forms near the loading boundary caused by boundary effects on instability. The direction of the loading is different with respect to the microstructural symmetry axes. Again, the evolution of ductile fracture also takes place more or less simultaneously in Figure 15(b). The stresses are not uniformly distributed and are especially low near the boundaries because of the lower local volume fraction. Even though the volume fraction of microstructure (B) is lower, the ductility is lower. This indicates that the overall volume fraction is not a good indicator of ductile fracture in that it does not adequately represent the local characteristics. Inclusion cracking is more dispersed for microstructure (D), which has a smaller minimum NND and higher *Cluster index* and *Contour index*. An interesting observation is that though the inclusion 1 in Figure 15 cracks early, it does not contribute to the dominant damage for the microstructure.

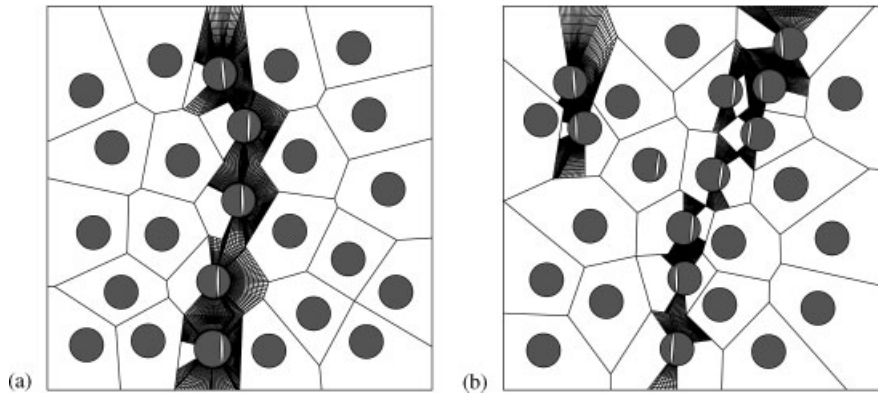


Figure 13. Voronoi cell model with locally enhanced displacement elements for the microstructures: (a) C and (b) D at strain to failure.

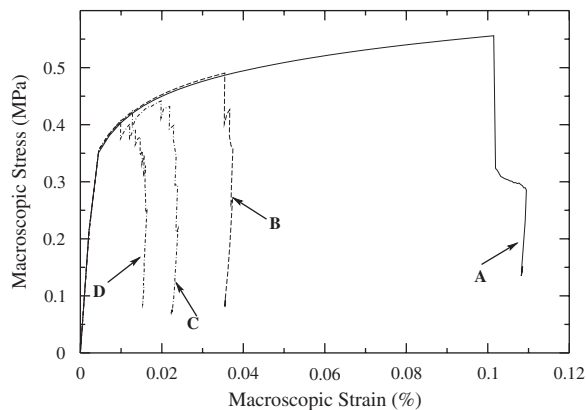


Figure 14. Macroscopic stress–strain response for the different microstructures.

Table VIII. Equivalent strains to failure for each microstructure.

Microstructure	(A)	(B)	(C)	(D)
Final equivalent strain	0.109	0.037	0.020	0.016

Figures 15(c) and (d) show that the inclusion cracking occurs mainly along the fracture path after the main ductile fracture path has formed. This example shows the effect of spatial distribution on ductility, especially the dominant damage path. Microstructural morphology and hence characterization functions alone are insufficient for predicting the damage path and strain to failure. However, in general, it is observed that the cluster contour index in Table VI is a good indicator

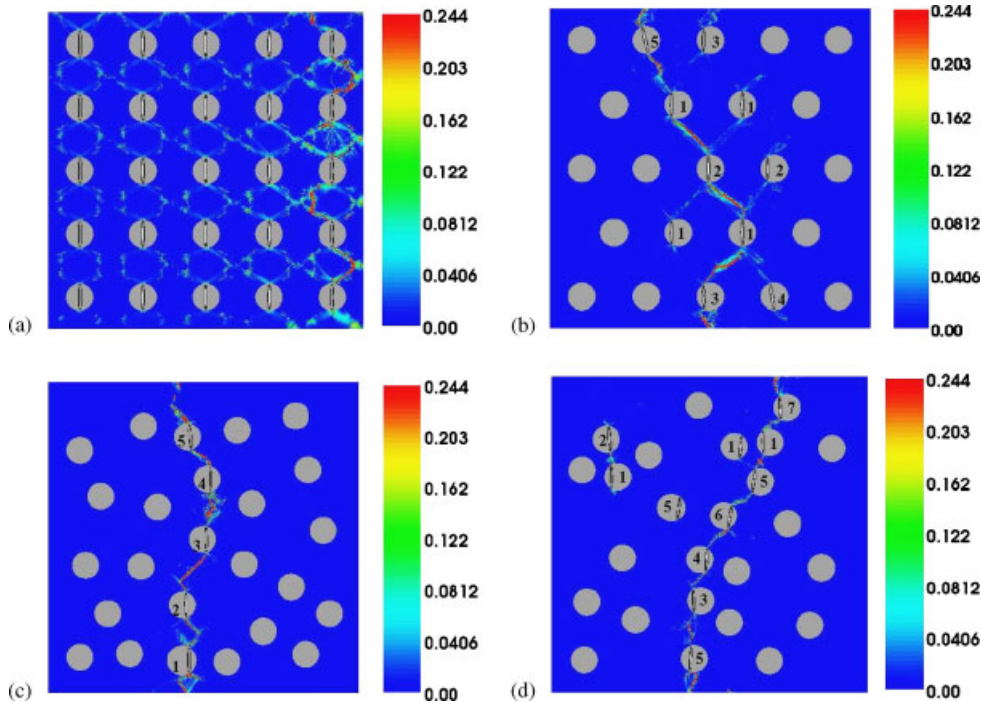


Figure 15. The contour plot of void volume fraction for microstructure: (A), (B), (C) and (D). The numbers in the figures indicate the sequence of particle cracking.

of the sequence of ductile fracture in the microstructures. In other words, ductility has an inverse relation to the contour index in these simulations.

5.2. Effect of porosity in plasticity relations on ductile failure

The effect void volume fraction in plastic flow representation on the material ductility is examined in this example with two sets of simulations. One is with the pressure-dependent GTN model for porous elasto-plastic material. The other uses incompressible J_2 plasticity model. The model in Figure 11(d) is used in this example. The material properties, crack nucleation properties and VCFEM parameters are similar to those in the previous example with the exception of the void and particle crack nucleation parameters $\varepsilon_N = 0.3$, $s_N = 0.1$, $f_N = 0.04$, $\sigma_w = 0.45$ GPa and $m = 2.4$ in the GTN and Weibull models.

Figure 16 shows the stress–strain response for the two simulations. There is no complete ductile failure with the J_2 plasticity model, with a near-stabilized stress value for increasing stress. The strain to failure with the GTN model is around $\bar{\varepsilon} = 0.02$. From the contour plot of effective plastic strain in Figure 17, it is seen that only five inclusions cracked for GTN model along the localized path of the dominant crack. A significant drop in the load-carrying capacity and instability occurs early on with matrix softening. On the other hand, almost all inclusions cracked in the J_2 plasticity model. Lack of matrix softening in this model causes only relocation of regions of high inclusion

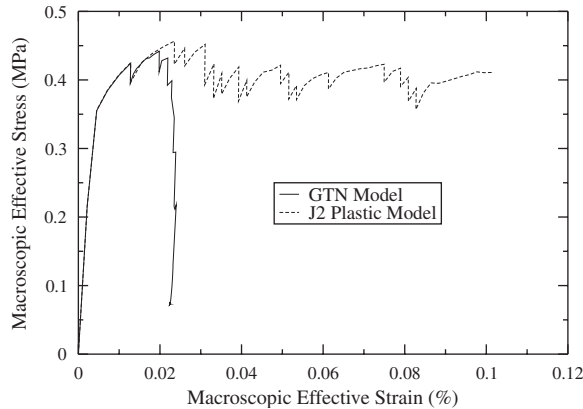


Figure 16. The macroscopic stress–strain response for GTN model and J_2 plasticity model.

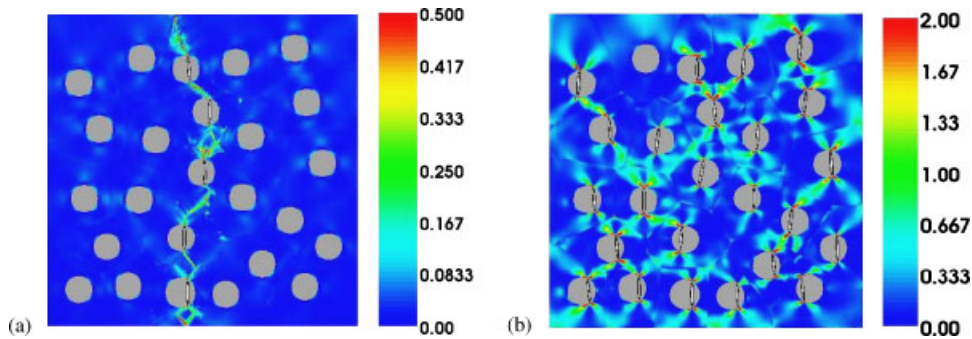


Figure 17. Contour plot of effective plastic strain for (a) the GTN model and (b) J_2 plasticity model.

stresses with subsequent cracking. Ductility predictions that are made using models such as the J_2 plasticity can be significantly in error with respect to real experimental observations.

5.3. Ductile fracture for a real microstructure

A two-dimensional VCFEM simulation of an experimental micrograph with inclusion cracking has been conducted only in [2]. As shown in Figure 18(a), the $195 \times 155.018 \mu\text{m}^2$ micrograph is a section of commercial X2080 aluminum alloy with 15% volume fraction SiC inclusions. The experiments in [2] consisted of uniaxial straining of a sample to failure followed by serial-sectioning to reveal failed microstructures. For example, the micrograph 18(a) is a section with a dominant crack. In this example, a complete ductile fracture analysis of the same experimental micrograph is conducted including both inclusion and matrix cracking. The micrograph is monotonically strained to failure. An equivalent VCFE model with elliptical inclusions that have the same zeroth, first and second area moments of inertia as particles in the experimental micrograph is shown in

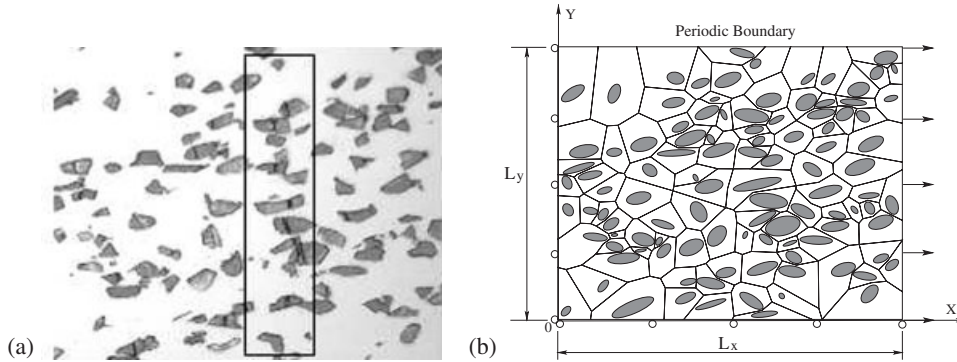


Figure 18. (a) Experimental micrograph and (b) VCFEM mesh with boundary conditions.

Figure 18(b). Periodicity boundary conditions are imposed by requiring edges to remain straight and parallel to the original direction throughout deformation as

$$\begin{aligned}
 u_x &= 0 \quad (\text{on } x=0), & u_y &= 0 \quad (\text{on } y=0), & u_x &= u_{\text{ap}} \quad (\text{on } x=L_x) \\
 u_y &= D_y^* \quad (\text{on } y=L_y), & T_y &= 0 \quad (\text{on } x=0/L_x), & T_x &= 0 \quad (\text{on } y=0/L_y)
 \end{aligned}$$

where u_{ap} is an applied displacement and D_y^* is determined from the average force condition $\int_X T_x dx = 0$ on $y=L_y$. The reinforcing phase of SiC inclusions is assumed to be brittle and is modeled with the linear elastic properties $E_{\text{SiC}} = 427 \text{ GPa}$, $\nu_{\text{SiC}} = 0.17$. The aluminum matrix material is assumed to be ductile and is modeled as porous material with properties Young's modulus $E_{\text{Al}} = 72 \text{ GPa}$, the Poisson ratio $\nu_{\text{Al}} = 0.33$. The post yield elastic–plastic response function is obtained from Figure 7(a) in Reference [2] and the initial void volume fraction is taken as $f_{\text{in}} = 0.001$. For the Weibull model, values $\sigma_w = 1.26 \text{ GPa}$, $m = 4.2$ have been calibrated in [2]. For the stress function, 33 polynomial terms (seventh-order polynomial stress function) with additional 36 reciprocal terms (three reciprocal terms for each polynomial exponent from 2 to 4, i.e. $i = p+q \dots p+q+2$, $\forall p+q = 2 \dots 4$) are used for matrix, and 33 polynomial terms are used for inclusion. After inclusion cracking, 36 reciprocal terms due to the crack shape are added into the inclusion stress function.

The solid line in Figure 19(a) corresponds to the experimental stress–strain response of the specimen. Only inclusion cracking is observed at early stages of deformation. Ductile fracture, which depends on localized plastic deformation, occurs later but very rapidly. The fracture strain in the experiment is about 8.88%. Owing to negligible void evolution at the early stages, a J_2 plasticity model with inclusion cracking only is considered for calibrating constitutive parameters in the pre-ductile damage macroscopic stress–strain response. VCFEM simulations are conducted under plane strain, plane stress and generalized plane strain conditions, respectively, to see which one fits the three-dimensional experimental response the best. As shown in Figure 19(a), neither the plane stress condition nor the plane strain condition gives a good match between VCFEM simulation and experiment results. However, the generalized plane strain condition with an out-of-plane strain $\varepsilon_{zz} = -0.005$ yields a good match with the experimental results. This generalized plane strain condition is accepted for subsequent simulations.

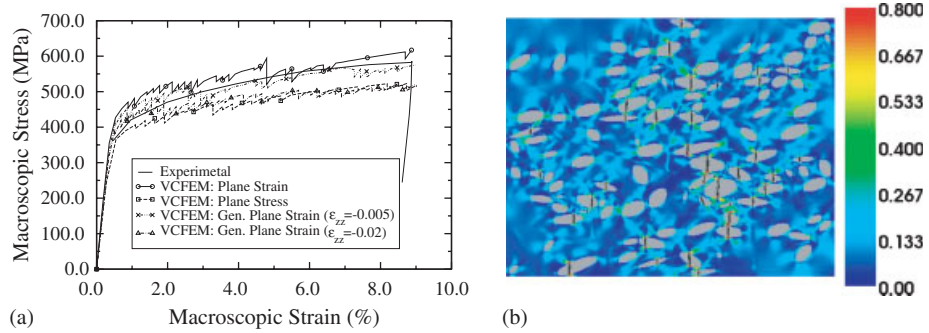


Figure 19. (a) Macroscopic stress–strain response and (b) contour plot of effective plastic strain at $\epsilon_{xx} = 8.88\%$, for the real microstructure modeled by VCFEM with J_2 plasticity and inclusion cracking.

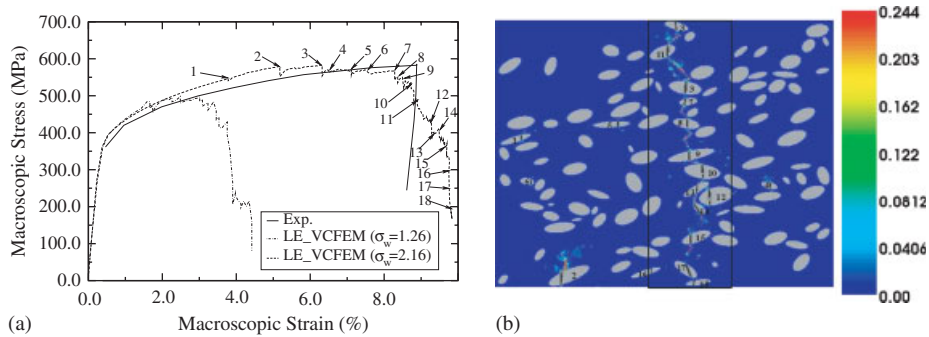


Figure 20. (a) Macroscopic stress–strain response from uniaxial experiments and LE-VCFEM simulations; (b) contour plot of void volume fraction at the strain to failure; and (c) Voronoi cell model with locally enhanced displacement elements for the real microstructure. (Numbers indicate the sequence of inclusion cracking.)

Results of a VCFEM simulation of the microstructure without any void nucleation or growth are shown in the contour plot of effective plastic strain in Figure 19(b). The effective plastic strain is greater than 0.5 in most regions near the tips of particle cracks. Consequently, the void

nucleation parameters are taken as $\varepsilon_N = 0.5$, $s_N = 0.075$ and $f_N = 0.08$, whereas $f_c = 0.15$, $f_f = 0.25$ for void coalescence in LE-VCFEM simulations. The average NND of particles in the micrograph is $L_{\text{NND}} = 3.2 \mu\text{m}$, and the same value is used for the material characteristic length, $\text{MCL} = 3.2 \mu\text{m}$. In [2], Weibull parameters $\sigma_w = 1.26 \text{ GPa}$, $m = 4.2$ were calibrated without any matrix cracking. If these values are used in LE-VCFEM, premature ductile failure occurs as shown in Figure 20. Localization due to matrix cracking can significantly change the final damage pattern, and hence a new set of Weibull parameters is evaluated by fitting the macroscopic stress–strain response with the experimental result. The exponent $m = 4.2$ is kept the same, as it is predominantly affected by the distribution of damaged inclusions. The calibrated new stress parameter is $\sigma_w = 2.16 \text{ GPa}$.

Figure 20(a) shows the macroscopic stress–strain response obtained by LE-VCFEM simulation with explicit delineation of inclusion cracking followed by ductile matrix fracture. The corresponding locally enhanced mesh and the contour plot of void volume fraction are shown in Figure 20(b). The first six inclusions crack in isolation and do not give rise to any major softening in the stress–strain behavior. Softening, manifested by a drop in the stress–strain curve, starts after the seventh inclusion has cracked followed by significant plastic deformation and void growth in the matrix. Figure 20(c) shows the Voronoi cell mesh with the locally enhanced displacement elements at the final strain. From the contour plot of void volume fraction in Figure 20(b), it is evident that subsequent inclusion and matrix cracking occur in a very narrow band and a clear dominant fracture path is observed. The dominant fracture zone in the LE-VCFEM simulation is shown by the boxed region of Figure 20(b). It matches the corresponding experimental fracture path of Figure 18(a) rather well.

6. CONCLUSIONS

This paper has incorporated adaptive local enhancement to the Voronoi cell finite element model (VCFEM) aimed at modeling ductile fracture in elastic–plastic heterogeneous microstructures. The assumed stress-based VCFEM has been developed for accurate and efficient micromechanical modeling of elastic–plastic deformation of heterogeneous microstructures. VCFEM is essentially a meshless method, as it does not require any discretization of the Voronoi cell that represents the immediate neighborhood or region of influence of a heterogeneity. Conventional VCFEM has been effective in modeling inclusion cracking, triggered by a Weibull criterion, in an elastic–plastic matrix. However, the stress-based formulation suffers inherent shortcomings when modeling ductile fracture that initiates with inclusion cracking and evolves in the matrix with void growth and coalescence. It faces numerical instabilities in the regime of strain softening due to nonuniqueness in strains for given values of stresses.

To overcome this shortcoming and also to provide a high resolution to the strain localization zone, a locally enhanced VCFEM (LE-VCFEM) is developed in this paper. In this method, regions of strain softening are adaptively augmented with patches of high-resolution displacement-based FEs, undergoing large localized deformation. Damage propagation and growth of ductile fracture in the matrix material are modeled by using a nonlocal GTN constitutive model with finite deformation kinematics. The LE-VCFEM is capable of modeling complete ductile failure of the microstructure from inclusion cracking to localized matrix cracking in the form of ligaments of void nucleation, growth and coalescence. Numerical validation of LE-VCFEM is established by comparing with results of commercial codes and experiments. Studies with different morphologies conclude that

morphological characterization alone is not sufficient for predicting the ductile fracture path and strain to failure. The interaction of evolving damage states plays an important role as well.

This paper conclusively demonstrates the potential of LE-VPFEM in modeling the challenging problem of ductile fracture in heterogeneous metallic materials. Such modeling has been very difficult with conventional FE models and often unreasonable shortcuts have been made for predicting ductile fracture. LE-VPFEM combines both accuracy and efficiency to deal with this complex class of problems and has excellent prospects as a material modeling tool for heterogeneous materials such as cast aluminum alloys. The limitation of the present model is that it is two dimensional and obviously has limited predictive capability with truly three-dimensional phenomena. It is expected that the three-dimensional models will be developed in the near future.

ACKNOWLEDGEMENTS

This study has been supported by the National Science Foundation NSF Div Civil and Mechanical Systems Division through the GOALI Grant No. CMS-0308666 (Program director: C. Cooper) and by the Department of Energy Aluminum Visions program through grant no. A5997. This sponsorship is gratefully acknowledged. Computer support by the Ohio Supercomputer Center through grant PAS813-2 is also gratefully acknowledged.

REFERENCES

1. Kiser M, Zok F, Wilkinson D. Plastic flow and fracture of a particulate metal matrix composite. *Acta Metallurgica et Materialia* 1996; **9**:3465–3476.
2. Li M, Ghosh S, Richmond O. An experimental-computational approach to the investigation of damage evolution in discontinuously reinforced aluminum matrix composite. *Acta Materialia* 1999; **47**:3515–3532.
3. Moorthy S, Ghosh S. A Voronoi cell finite element model for particle cracking in elastic–plastic composite materials. *Computer Methods in Applied Mechanics and Engineering* 1998; **151**:377–400.
4. Poole W, Dowdle E. Experimental measurements of damage evolution in Al–Si eutectic alloys. *Scripta Materialia* 1998; **39**:1281–1287.
5. Wang Q. Microstructural effects on the tensile and fracture behavior of aluminum casting alloys A356/357. *Metallurgical and Materials Transactions A* 2003; **34A**:2887–2899.
6. Argon A, Im J, Sofoglu R. Cavity formation from inclusions in ductile fracture. *Metallurgical Transactions A* 1975; **6A**:825–837.
7. Caceres C. Particle cracking and the tensile ductility of a model Al–Si–Mg composite system. *Aluminum Transactions* 1999; **1**:1–13.
8. Finot M, Shen Y, Needleman A, Suresh S. Micromechanical modeling of reinforcement fracture in particle-reinforced metal–matrix composites. *Metallurgical and Materials Transactions A* 1994; **25**:2403–2420.
9. Needleman A. An analysis of decohesion along an imperfect interface. *International Journal of Fracture* 1990; **42**:21–40.
10. Siegmund T, Brocks W. Prediction of the work of separation and implications to modeling. *International Journal of Fracture* 1999; **99**:97–116.
11. Tvergaard V, Hutchinson J. Effect of strain-dependent cohesive zone model on predictions of crack growth resistance. *International Journal of Solids and Structures* 1996; **33**:3297–3308.
12. Gurson A. Continuum theory of ductile rupture by void nucleation and growth. *Engineering Material Technology* 1977; **99**:2–15.
13. Tvergaard V, Needleman A. Analysis of cup–cone fracture in a round tensile bar. *Acta Metallurgica* 1984; **32**:157–169.
14. Benzerga A, Besson J, Pineau A. Coalescence-controlled anisotropic ductile fracture. *Journal of Engineering Materials and Technology* 1999; **121**:221–229.
15. Gologanu M, Leblond J, Devaux J. Approximate models for ductile metals containing nonspherical voids—case of axisymmetric oblate ellipsoidal cavities. *Journal of Engineering Materials and Technology* 1994; **116**:290–297.

16. Pardoën T, Hutchinson J. An extended model for void growth and coalescence. *Journal of the Mechanics and Physics of Solids* 2000; **48**:2467–2512.
17. Hao S, Brocks W. The Gurson–Tvergaard–Needleman-model for rate and temperature-dependent materials with isotropic and kinematic hardening. *Computational Mechanics* 1997; **20**:34–40.
18. Benzerga A, Besson J, Pineau A. Anisotropic ductile fracture. Part II: Theory. *Acta Metallurgica* 2004; **52**:4639–4650.
19. Tvergaard V. Influence of void nucleation on ductile shear fracture at a free surface. *Journal of the Mechanics and Physics of Solids* 1982; **30**:399–425.
20. Pan J, Saje M, Needleman A. Localization of deformation in rate sensitive porous plastic solids. *International Journal of Fracture* 1983; **21**:261–278.
21. Needleman A, Tvergaard V. An analysis of ductile rupture modes at a crack tip. *Journal of the Mechanics and Physics of Solids* 1987; **35**:151–183.
22. Chu C, Needleman A. Void nucleation effects in biaxially stretched sheets. *Journal of Engineering Materials and Technology* 1980; **102**:249–256.
23. Tvergaard V, Needleman A. Nonlocal effects on localization in a void-sheet. *International Journal of Solids and Structures* 1997; **34**:2221–2238.
24. Koplik J, Needleman A. Void growth and coalescence in porous plastic solids. *International Journal of Solids and Structures* 1988; **24**:835–853.
25. Benzerga A, Besson J, Batisse R, Pineau A. Synergistic effects of plastic anisotropy and void coalescence on fracture mode in plane strain. *Modelling and Simulation in Material Science and Engineering* 2002; **10**:73–102.
26. Tvergaard V, Needleman A. Effect of nonlocal damage in porous plastic solids. *International Journal of Solids and Structures* 1995; **32**:1063–1077.
27. Ghosal A, Narasimhan R. Mixed-mode fracture initiation in a ductile material with a dual population of second-phase particles. *Materials Science and Engineering* 1996; **A211**:117–127.
28. Steglich D, Brocks W. Micromechanical modeling of the behavior of ductile materials including particles. *Computational Materials Science* 1997; **9**:7–17.
29. Lim L, Dunne F. Modeling void nucleation and growth processes in a particle-reinforced metal matrix composite material. *Computational Materials Science* 1996; **5**:177–186.
30. Negre P, Steglich D, Brocks W, Kocak M. Numerical simulation of crack extension in aluminium welds. *Computational Materials Science* 2003; **28**:723–731.
31. Huber G, Brechet Y, Pardoën T. Predictive model for void nucleation and void growth controlled ductility in quasi-eutectic cast aluminium alloys. *Acta Materialia* 2005; **53**:2739–2749.
32. Llorca J, Gonzalez C. Microstructural factors controlling the strength and ductility of particle-reinforced metal-matrix composites. *Journal of the Mechanics and Physics of Solids* 1998; **46**:1–28.
33. Llorca J, Segurado J. Three-dimensional multiparticle cell simulations of deformation and damage in sphere-reinforced composites. *Materials Science and Engineering* 2004; **A365**:267–274.
34. Jirasek M. A comparative study on finite elements with embedded discontinuities. *Computer Methods in Applied Mechanics and Engineering* 2000; **188**(1):307–330.
35. Needleman A. Micromechanical modeling of interfacial decohesion. *Ultramicroscopy* 1992; **40**:203–214.
36. Geubelle P. Finite deformation effects in homogeneous and interfacial fracture. *International Journal of Solids and Structures* 1995; **32**:1003–1016.
37. Camacho G, Ortiz M. Computational modeling of impact damage in brittle materials. *International Journal of Solids and Structures* 1996; **33**:2899–2938.
38. Ortiz M, Leroy Y, Needleman A. A finite element method for localized failure analysis. *Computer Methods in Applied Mechanics and Engineering* 1987; **61**:189–214.
39. Belytschko T, Fish J, Engelmann B. A finite element with embedded localization zones. *Computer Methods in Applied Mechanics and Engineering* 1988; **70**:59–89.
40. Fish J, Markolefas S. Adaptive S-method for linear elastostatics. *Computer Methods in Applied Mechanics and Engineering* 1993; **103**:363–396.
41. Simo J, Rifai M. A class of mixed assumed strain methods and the method of incompatible modes. *International Journal for Numerical Methods in Engineering* 1990; **29**:1595–1638.
42. Simo J, Armero F. Geometrically non-linear enhanced strain mixed methods and the method of incompatible modes. *International Journal for Numerical Methods in Engineering* 1992; **33**:1413–1449.
43. Simo J, Oliver J. A new approach to the analysis and simulation of strain softening in solids. In *Fracture and Damage in Quasibrittle Structures*, Bazant Z, Bittnar Z, Jirasek M, Mazars J (eds). E FN Spon: London, 1994; 25–39.

44. Belytschko T, Krongauz Y, Organ D, Fleming M, Krysl P. Meshless methods: an overview and recent developments. *Computer Methods in Applied Mechanics and Engineering* 1996; **139**:3–47.
45. Belytschko T, Black T. Elastic crack growth in finite elements with minimal remeshing. *International Journal for Numerical Methods in Engineering* 1999; **45**:601–620.
46. Moes N, Belytschko T. Extended finite element method for cohesive crack growth. *Engineering Fracture Mechanics* 2002; **69**:813–833.
47. Moorthy S, Ghosh S. Adaptivity and convergence in the Voronoi cell finite element model for analyzing heterogeneous materials. *Computer Methods in Applied Mechanics and Engineering* 2000; **185**:37–74.
48. Ghosh S, Ling Y, Majumdar B, Kim R. Interfacial debonding analysis in multiple fiber reinforced composites. *Mechanics of Materials* 2000; **32**:561–591.
49. Li S, Ghosh S. Extended Voronoi cell finite element model for multiple cohesive crack propagation in brittle materials. *International Journal for Numerical Methods in Engineering* 2006; **65**:1028–1067.
50. Li S, Ghosh S. Multiple cohesive crack growth in brittle materials by the extended Voronoi cell finite element model. *International Journal of Fracture* 2006; **141**:373–393.
51. Ghosh S, Moorthy S. Particle fracture simulation in non-uniform microstructures of metal–matrix composites. *Acta Materialia* 1998; **46**:965–982.
52. Moorthy S, Ghosh S. A model for analysis of arbitrary composite and porous microstructures with Voronoi cell finite elements. *International Journal for Numerical Methods in Engineering* 1996; **39**:2363–2398.
53. Driscoll T, Trefethen L. *Schwarz–Christoffel Mapping*. Cambridge University Press: Cambridge, 2002.
54. Tvergaard V. Influence of voids on shear band instabilities under plane strain conditions. *International Journal of Fracture Mechanics* 1981; **17**:389–407.
55. Leblond J, Perrin G, Devaux J. Bifurcation effects in ductile metals with damage delocalization. *Journal of Applied Mechanics* 1994; **61**:236–242.
56. Aravas N. On the numerical integration of a class of pressure-dependent plasticity models. *International Journal for Numerical Methods in Engineering* 1987; **24**:1395–1416.
57. Ortiz M, Simo J. An analysis of a new class of integration algorithms for elastoplastic constitutive equations. *International Journal for Numerical Methods in Engineering* 1986; **23**:353–366.
58. Robinson S. Interpolative solution of systems of nonlinear equations. *SIAM Journal on Numerical Analysis* 1966; **3**(4):650–658.
59. Hu C. Locally enhanced Voronoi cell finite element model (LE-VCFEM) for ductile fracture in heterogeneous cast aluminum alloys. *Ph.D. Thesis*, The Ohio State University, 2007.
60. Harris S, O’Neill A, Boileau J, Donlon W, Su X, Majumdar B. Application of the Raman technique to measure stress states in individual Si particles in a cast Al–Si alloy. *Acta Materialia* 2007; **55**:1681–1693.
61. Harris S, O’Neill A, Yang W, Gustafson P, Boileau J, Weber W, Majumdar B, Ghosh S. Measurement of the state of stress in silicon with micro-Raman spectroscopy. *Journal of Applied Physics* 2004; **96**:7195–7201.
62. Beremin F. A local criterion for cleavage fracture of a nuclear pressure vessel steel. *Metallurgical and Materials Transactions A* 1983; **14**:2277–2287.
63. Zienkiewicz O, Zhu J. The superconvergent patch recovery and a posteriori error estimates. Part 1: the recovery technique. *International Journal for Numerical Methods in Engineering* 1992; **33**:1331–1364.
64. Ghosh S, Kikuchi N. An arbitrary Lagrangian–Eulerian finite element method for large deformation analysis of elastic–viscoplastic solids. *Computer Methods in Applied Mechanics and Engineering* 1991; **86**:127–188.
65. Green A, Naghdi P. A general theory of an elastic–plastic continuum. *Archive for Rational Mechanics and Analysis* 1965; **18**:251–281.
66. Hughes T. Generalization of selective integration procedures to anisotropic and nonlinear media. *International Journal for Numerical Methods in Engineering* 1980; **15**:1413–1418.
67. Crisfield M. An arc-length method including line searches and accelerations. *International Journal for Numerical Methods in Engineering* 1983; **19**:1269–1289.
68. Bass J, Oden J. Adaptive finite element methods for a class of evolution problems in viscoplasticity. *International Journal of Engineering Science* 1987; **6**:623–653.
69. Ghosh S, Valiveti DM, Harris SJ, Boileau J. A domain partitioning based pre-processor for multi-scale modeling of cast aluminum alloys. *Modeling and Simulation in Materials Science and Engineering* 2006; **14**:1363–1396.